



LJMU Research Online

Fong, M, Choi, M, Catlett, V, Lee, B, Peel, A, Bowyer, R, King, LJ and McCarthy, IG

The impact of baryonic physics and massive neutrinos on weak lensing peak statistics

<http://researchonline.ljmu.ac.uk/id/eprint/11068/>

Article

Citation (please note it is advisable to refer to the publisher's version if you intend to cite from this work)

Fong, M, Choi, M, Catlett, V, Lee, B, Peel, A, Bowyer, R, King, LJ and McCarthy, IG (2019) The impact of baryonic physics and massive neutrinos on weak lensing peak statistics. Monthly Notices of the Royal Astronomical Society. 488 (3). pp. 3340-3357. ISSN 0035-8711

LJMU has developed [LJMU Research Online](#) for users to access the research output of the University more effectively. Copyright © and Moral Rights for the papers on this site are retained by the individual authors and/or other copyright owners. Users may download and/or print one copy of any article(s) in LJMU Research Online to facilitate their private study or for non-commercial research. You may not engage in further distribution of the material or use it for any profit-making activities or any commercial gain.

The version presented here may differ from the published version or from the version of the record. Please see the repository URL above for details on accessing the published version and note that access may require a subscription.

For more information please contact researchonline@ljmu.ac.uk

<http://researchonline.ljmu.ac.uk/>

The impact of baryonic physics and massive neutrinos on weak lensing peak statistics

Matthew Fong,^{1★} Miyoung Choi,^{1★} Victoria Catlett,¹ Brandyn Lee,¹ Austin Peel,²
Rachel Bowyer,³ Lindsay J. King^{1★} and Ian G. McCarthy⁴ 

¹Physics Department, The University of Texas at Dallas, 800 W. Campbell Road, Richardson, TX 75080, USA

²AIM, CEA, CNRS, Université Paris-Saclay, Université Paris Diderot, Sorbonne Paris Cité, F-91191 Gif-sur-Yvette, France

³Department of Astrophysical and Planetary Sciences, 391 UCB, University of Colorado, Boulder, CO 80309-0391, USA

⁴Astrophysics Research Institute, Liverpool John Moores University, 146 Brownlow Hill, Liverpool L3 5RF, UK

Accepted 2019 June 28. Received 2019 June 28; in original form 2019 March 26

ABSTRACT

We study the impact of baryonic processes and massive neutrinos on weak lensing peak statistics that can be used to constrain cosmological parameters. We use the BAHAMAS suite of cosmological simulations, which self-consistently include baryonic processes and the effect of massive neutrino free-streaming on the evolution of structure formation. We construct synthetic weak lensing catalogues by ray tracing through light-cones, and use the aperture mass statistic for the analysis. The peaks detected on the maps reflect the cumulative signal from massive bound objects and general large-scale structure. We present the first study of weak lensing peaks in simulations that include both baryonic physics and massive neutrinos (summed neutrino mass $M_\nu = 0.06, 0.12, 0.24,$ and 0.48 eV assuming normal hierarchy), so that the uncertainty due to physics beyond the gravity of dark matter can be factored into constraints on cosmological models. Assuming a fiducial model of baryonic physics, we also investigate the correlation between peaks and massive haloes, over a range of summed neutrino mass values. As higher neutrino mass tends to suppress the formation of massive structures in the Universe, the halo mass function and lensing peak counts are therefore modified as a function of M_ν . Over most of the S/N range, the impact of fiducial baryonic physics is greater (less) than neutrinos for 0.06 and 0.12 (0.24 and 0.48) eV models. Both baryonic physics and massive neutrinos should be accounted for when deriving cosmological parameters from weak lensing observations.

Key words: gravitational lensing: weak – neutrinos – large-scale structure of Universe – cosmology: theory.

1 INTRODUCTION

Galaxy clusters and large-scale structure (LSS) provide a powerful laboratory to study the Universe (e.g. Bond, Efstathiou & Silk 1980; Blumenthal et al. 1984; Voit 2005; Allen, Evrard & Mantz 2011; Kravtsov & Borgani 2012). Measurements of LSS help constrain cosmological parameters, independent from observations of the cosmic microwave background (CMB), and other probes.

Agreement between various astrophysical probes has provided strong evidence for a concordance cosmology, the Λ CDM model (Λ cold dark matter). However, recent high-precision measurements have suggested a tension in some of the parameter estimates.

For example, some authors have determined that local measurements of Hubble’s constant H_0 (73.48 ± 1.66 km s^{−1} Mpc^{−1}, Riess et al. 2018) disagree with the value derived from the joint analysis of CMB and baryon acoustic oscillations (BAOs) (67.4 ± 0.5 km s^{−1} Mpc^{−1}; Planck Collaboration VI 2018). However some analyses have suggested that the discrepancy between the measurements is of low significance. For example, Feeney, Mortlock & Dalmaso (2018) developed a Bayesian hierarchical model of the distance ladder that finds a local H_0 value nearly identical to the *Planck* CMB measurement. Another tension that has been found by some studies is between measurements of Ω_m and of σ_8 , the present-day matter density of the Universe and the density perturbation amplitude on $8 h^{-1}$ Mpc scale (see for example the discussion in Hildebrandt et al. 2017; McCarthy et al. 2018; Planck Collaboration VI 2018), where h is H_0 scaled by 100 km s^{−1} Mpc^{−1}.

* E-mail: Matthew.Fong@utdallas.edu (MF); Miyoung.Choi@utdallas.edu (MC); Lindsay.King@utdallas.edu (LJK)

Traditionally, simulations of cosmological structure formation have considered only collisionless gravitational dynamics. However, with the increase in computational capabilities, some large-volume simulations have now been carried out to model LSS for various cosmologies and using various prescriptions for baryonic physics (e.g. Dolag et al. 2009; Schaye et al. 2010; Vogelsberger et al. 2013; Dubois et al. 2014; Le Brun et al. 2014; Schaye et al. 2015; McCarthy et al. 2017; Pillepich et al. 2018). These and other simulations have shown that baryonic physics affects the total matter power spectrum (e.g. Semboloni et al. 2011; van Daalen et al. 2011; Schneider & Teyssier 2015), one-point lensing statistics (Castro et al. 2018), the halo mass function (e.g. Sawala et al. 2013; Cusworth et al. 2014; Velliscig et al. 2014), and galaxy cluster density profiles and mass estimation (e.g. Schaller et al. 2015; Henson et al. 2017; Mummery et al. 2017; Lee et al. 2018). For example, on galaxy and cluster scales baryonic feedback produces an outward pressure that acts against the infall of matter, resulting in a shallower inner density profile, corresponding to a lower concentration of mass (Mummery et al. 2017). For the ongoing 1400 deg² Subaru Hyper Suprime-Cam survey, Osato, Shirasaki & Yoshida (2015) estimate that when the peak statistics, or other lensing statistics are used alone, the parameter bias due to baryonic physics is not significant with most of the biased parameters lying within the 1σ error. However this would not be the case for a survey covering a larger fraction of the sky. These works have illustrated that the addition of baryons can have a significant impact on our inference of cosmological parameters.

Neutrinos are the most ubiquitous subatomic particle in the Universe. Massive neutrinos act like a form of hot dark matter. The high speeds of neutrinos at early times tend to resist gravitational collapse and to impede the growth of structure, while cold dark matter facilitates structure formation. Theoretical and observational studies of the impact of neutrinos on cosmological structure formation have been carried out by e.g. Hu, Eisenstein & Tegmark (1998), Bashinsky & Seljak (2004), Hannestad, Tu & Wong (2006), Gratton, Lewis & Efstathiou (2008), Namikawa, Saito & Taruya (2010), Lahav et al. (2010), Bird, Viel & Haehnelt (2012), Wagner, Verde & Jimenez (2012), Costanzi et al. (2013), Villaescusa-Navarro et al. (2014), Castorina et al. (2014), Roncarelli, Carbone & Moscardini (2015), Mummery et al. (2017), Moscardini, Baldi & Giocoli (2018), and Hagstotz et al. (2019). However, their mass is not yet known, and the relevance of massive neutrinos to structure formation and to astrophysical observables is an open question. Lesgourgues & Pastor (2006) found that the three active neutrino species have a summed mass of at least 0.06 eV for normal or inverted hierarchies, by studying atmospheric and solar oscillation experiments. In their fiducial analysis, Planck Collaboration XIII (2016a) adopt a value of $M_\nu = 0.06$ eV. The CMB data itself can be used to constrain the summed neutrino mass and, when combined with external BAO constraints, Planck Collaboration XIII (2016a) set an upper limit of $M_\nu < 0.21$ eV. However, the derived upper limit is sensitive to the treatment of internal tensions in the primary CMB data (e.g. Addison et al. 2016; Planck Collaboration LI 2017) and, when this is factored in, values of up to 0.4 eV are potentially compatible with the data (e.g. Di Valentino et al. 2017; McCarthy et al. 2018; Poulin et al. 2018).

Some studies find that the aforementioned tension in cosmological parameter measurements can potentially be remedied with the inclusion of massive neutrinos (e.g. Battye & Moss 2014; Wyman et al. 2014; McCarthy et al. 2018). Mummery et al. (2017) used cosmo-OWLS (the Overwhelmingly Large Simulations; Le Brun et al. 2014) and BAHAMAS (Baryons and HALoes of MAssive Systems; McCarthy et al. 2018) to study how baryonic physics

and neutrinos impact the halo mass function, mass density profiles of haloes, the halo mass–concentration relation, and the clustering properties of haloes.

The impact of baryonic physics and massive neutrinos is thought to be significant and has been considered as a systematic in various works on weak lensing (WL) statistics with dark matter only simulations and observational surveys (e.g. Yang et al. 2013; Hildebrandt et al. 2017; Martinet et al. 2018). In this work we are motivated by the studies above that suggest the importance of physics beyond the gravity associated with cold dark matter.

The statistics of the peaks on weak gravitational lensing maps has been shown to be a powerful probe of cosmology and massive galaxy clusters (e.g. Kruse & Schneider 1999, 2000; Jain & Waerbeke 2000; Dietrich & Hartlap 2010; Fan, Shan & Liu 2010; Kratochvil, Haiman & May 2010; Maturi et al. 2010; Yang et al. 2011; Hamana et al. 2012; Lin & Kilbinger 2015; Martinet et al. 2015; Kacprzak et al. 2016; Liu & Haiman 2016; Liu et al. 2016; Peel et al. 2017, 2018; Martinet et al. 2018; Shan et al. 2018; Davies, Cautun & Li 2019; Li et al. 2019). WL peaks arise from massive structures such as galaxy clusters but also from the LSS of the Universe. Thus, the peak statistics contain information about the Universe on both non-linear and linear scales (e.g. Yang et al. 2011; Liu & Haiman 2016; Martinet et al. 2018).

In this paper, we estimate the impact that baryons and massive neutrinos have on the counts of weak gravitational lensing peaks. The cosmological hydrodynamical simulations that we use in this work is BAHAMAS, a suite that includes the effects of massive neutrinos and for which the efficiencies of stellar and active galactic nuclei (AGNs) feedback have been carefully calibrated to match the observed baryon fractions of massive systems (McCarthy et al. 2017). For each run we use light-cones from BAHAMAS and generate sets of synthetic WL surveys with different source redshift distributions and source number densities for galaxies from which the WL signal is measured. The synthetic surveys used in this work are based on the Kilo Degree Survey (KiDS; de Jong et al. 2017; Hildebrandt et al. 2017), and on Deep Ground Based and Deep Spaced Based survey characteristics, such as expected for the Large Synoptic Survey Telescope (LSST; Chang et al. 2013) and *Euclid* (e.g. Laureijs et al. 2011; Amendola et al. 2018) and for the *Hubble Space Telescope* (*HST*; e.g. the WL observations in King et al. 2016), respectively. We consider surveys of the same size area as each other (625 deg²). We determine peaks on maps of the aperture mass statistic (Schneider 1996), as applied and adapted in e.g. Schneider et al. (1998), Schirmer et al. (2007), and Maturi et al. (2010).

The impact of baryonic physics on WL peak statistics has been studied (e.g. Osato et al. 2015; Castro et al. 2018) as well as the impact of summed neutrino mass (e.g. Peel et al. 2018; Li et al. 2019; Liu & Madhavacheril 2019), but never their combination as explored in this paper. We explore the impact of a range of different baryonic physics prescriptions on the statistics of the signal-to-noise (S/N) peaks, compared with the statistics of the peaks in dark matter only simulations with collisionless dynamics. For a fiducial baryonic physics model, we explore the impact of massive neutrinos; the lower bound of the summed neutrino mass in BAHAMAS is taken from Lesgourgues & Pastor (2006), with additional runs increasing the summed neutrino mass by factors of 2 up to 0.48 eV. Using a fiducial baryonic prescription outlined in Section 3, we also examine the correlation between high S/N peaks and massive galaxy clusters and assess our ability to detect clusters using aperture mass peaks. As far as we know, our work is the first systematic study of WL peaks using simulations which incorporate massive neutrinos in concert with

baryonic physics. A consideration of a broad range of cosmological models has been explored for S/N peak distributions (e.g. Yang et al. 2011; Liu & Haiman 2016; Liu et al. 2016; Martinet et al. 2018; Peel et al. 2018) but these simulations and other works do not include both the impact of summed neutrino mass and baryonic physics. In this paper we focus on baryonic physics and massive neutrinos and restrict our consideration to the two sets of cosmologies of BAHAMAS based on the *WMAP* 9-yr mission (*WMAP* 9; Hinshaw et al. 2013) and the Planck 2015 mission (*Planck* 2015; Planck Collaboration XVI 2016b) parameters.

The remainder of the paper is organized as follows: in Section 2 we introduce weak gravitational lensing. In Section 3 we outline the BAHAMAS simulation and how we generate synthetic lensing catalogues. In Section 4 we introduce how we quantify WL signatures using the aperture mass statistic and S/N peaks. In Section 5 we present the results on the impact of baryonic physics and summed neutrino mass on the S/N peak statistics. We also consider how summed neutrino mass affects the cluster mass function, mass of individual galaxy clusters, and the correlation between peak detection and cluster mass. In Section 6 we present a summary of our findings and conclude.

2 GRAVITATIONAL LENSING

The light bundles from distant background sources are distorted as they pass through the gravitational fields of massive objects and the general LSS. This distortion can be determined in general relativity, where light bundles follow null geodesics of the space-time metric that is distorted by mass. Cosmological simulations of structure formation for particular cosmological models provide a description of the distribution of mass in the Universe. In this section we introduce concepts of gravitational lensing relevant to the analysis of cosmological simulations.

The distorted appearance of the weakly lensed images of distant sources can be described by lensing convergence and shear. The WL calculations here assume the so-called ‘Born approximation’, where the paths of light rays are approximated as straight lines in comoving coordinates. This has been shown to be accurate for WL (e.g. Bartelmann & Schneider 2001; White & Vale 2004). In a given cosmological model, the WL convergence at a particular angular position, $\kappa(\theta)$, depends on the spatial distribution of mass density fluctuations, δ , in the Universe, and the redshift distribution of sources that are being lensed by the fluctuations, $p_s(z)$:

$$\kappa(\theta) = \frac{3\Omega_m H_0^2}{2c^2} \int_0^{\chi(z_{\max})} (1+z)s(\chi)\delta(\chi, \theta) d\chi, \quad (1)$$

where c is the speed of light, χ is the cosmological comoving distance, and $s(\chi)$ is a lensing kernel defined as

$$s(\chi) = \chi(z) \int_z^{z_{\max}} p_s(z') \left(\frac{\chi(z') - \chi(z)}{\chi(z')} \right) dz'. \quad (2)$$

The lensing kernel depends on the source redshift probability distribution, $p_s(z)$, where the maximum source redshift is z_{\max} and the distribution is normalized to 1. The light-cones we use from BAHAMAS extend out to $z_{\max} = 3$. The lensing convergence results in an isotropic distortion of a lensed source.

Given a map of the WL convergence, the complex shear, $\gamma = \gamma_1 + i\gamma_2$, can be obtained using Fourier transform techniques since both the convergence and shear can be written as linear combinations of second derivatives of the lensing potential. Following e.g. Clowe,

De Lucia & King (2004):

$$\tilde{\gamma} = \left(\frac{\hat{k}_1^2 - \hat{k}_2^2}{\hat{k}_1^2 + \hat{k}_2^2} \tilde{\kappa}, \frac{2\hat{k}_1\hat{k}_2}{\hat{k}_1^2 + \hat{k}_2^2} \tilde{\kappa} \right), \quad (3)$$

where $\tilde{\gamma}$ and $\tilde{\kappa}$ are the Fourier transforms of the complex shear and scalar convergence, and \hat{k} are wave vectors in Fourier space. The inverse Fourier transform of $\tilde{\gamma}$ yields γ , and the complex reduced shear g is given by $\gamma/(1-\kappa)$ which can also be written as

$$g = g_1 + ig_2 = |g|e^{2i\phi}, \quad (4)$$

where ϕ is the phase angle of the distortion and $|g|$ is related to the strength of the shear. The shear or reduced shear results in an anisotropic distortion of the lensed source.

Maps of the convergence and reduced shear are determined from the mass distributions in cosmological simulations as detailed in the next section.¹ These maps can then be used to determine the shapes of lensed galaxies. The shapes and orientation angles of the unlensed and lensed sources can be expressed as complex ellipticities ϵ^s and ϵ , respectively. The phase of a complex ellipticity is twice the orientation angle of the galaxy on the sky and the modulus of the complex ellipticity is related to the axial ratio through $\frac{1-b/a}{1+b/a}$, where a and b are the major and minor axes.

The intrinsic shape of a galaxy can be expressed as

$$\epsilon^s = |\epsilon^s|e^{2i\phi^s} \equiv \epsilon_1^s + i\epsilon_2^s, \quad (5)$$

where ϵ_1^s and ϵ_2^s are complex components of the source ellipticity $|\epsilon^s|\cos(2\phi^s)$ and $|\epsilon^s|\sin(2\phi^s)$ respectively and ϕ^s is the orientation of the source galaxy.

If a background source galaxy is circular, or $\epsilon^s = 0$, then the lensed galaxy ellipticity will be exactly $\epsilon = g$. In general, for non-critical lenses, the lensed and unlensed ellipticities are related by (e.g. Bartelmann 1996; Schneider et al. 1998; Schneider 2005):

$$\epsilon = \frac{\epsilon^s + g}{1 + g^*\epsilon^s} \equiv \epsilon_1 + i\epsilon_2, \quad (6)$$

where $*$ denotes taking the complex conjugate.

3 SYNTHETIC LENSING CATALOGUES: BAHAMAS SIMULATIONS

We use light-cones extracted from BAHAMAS (McCarthy et al. 2017). Motivated by the fact that neutrinos are massive and by the tension between cosmological parameter estimates from the LSS and the primary CMB, BAHAMAS allows for a range of non-zero neutrino masses (McCarthy et al. 2018). BAHAMAS is the only suite of cosmological hydrodynamical simulations that have been explicitly calibrated on the baryon fractions of collapsed systems. This guarantees that the response of the redistribution of total matter due to baryonic physics is broadly correct (see table 1 of McCarthy et al. 2017). In this section we will discuss the different runs with varying cosmology and neutrino mass that we use. We also discuss the creation of synthetic light-cones and WL galaxy catalogues used in our study.

3.1 Cosmology, neutrino mass, and baryonic physics

The initial conditions for BAHAMAS are based on the cosmological parameters derived from the cosmic microwave background

¹The publicly available BAHAMAS convergence and shear maps can be found at <http://www.astro.ljmu.ac.uk/igm/BAHAMAS/>

Table 1. Cosmological parameter values for 12 suites of the BAHAMAS simulations (McCarthy et al. 2017, 2018). Adjustments on the summed neutrino mass, baryonic matter fractions, AGN feedback temperatures, σ_8 values, and changes in S_8 are given in this table. The columns are: (1) The summed mass of the three active neutrino species (we adopt a normal hierarchy for the individual masses). Note that there is underlying fiducial baryonic physics for every non-zero M_ν model; (2) the logarithm to base 10 of the AGN feedback temperature defined by McCarthy et al. (2018); (3) the total matter density; (4) present-day baryon density; (5) present-day dark matter density; (6) present-day neutrino density, computed as $\Omega_\nu = M_\nu/(93.14 \text{ eV } h^2)$; (7) present-day (linearly evolved) amplitude of the matter power spectrum on a scale of $8 \text{ Mpc } h^{-1}$ (note that we use A_s rather than σ_8 to compute the power spectrum used for the initial conditions, thus the initial conditions are CMB normalized); (8) $S_8 = \sigma_8 \sqrt{\Omega_m}/0.3$.

(1)	(2)	(3)	(4)	(5)	(6)	(7)	(8)
M_ν (eV)	$\log(\Delta T_{\text{heat}}[\text{K}])$	Ω_m	Ω_b	Ω_{cdm}	Ω_ν	σ_8	S_8
WMAP 9-based							
0 (DMONLY)	–	0.2793	0.0463	0.2330	0.0	0.8211	0.7923
0 (low AGN)	7.6	0.2793	0.0463	0.2330	0.0	0.8211	0.7923
0 (fiducial AGN)	7.8	0.2793	0.0463	0.2330	0.0	0.8211	0.7923
0 (high AGN)	8.0	0.2793	0.0463	0.2330	0.0	0.8211	0.7923
0.06	7.8	0.2793	0.0463	0.2317	0.0013	0.8069	0.7786
0.12	7.8	0.2793	0.0463	0.2304	0.0026	0.7924	0.7646
0.24	7.8	0.2793	0.0463	0.2277	0.0053	0.7600	0.7333
0.48	7.8	0.2793	0.0463	0.2225	0.0105	0.7001	0.6755
Planck2015/A_{Lens}-based							
0.06	7.8	0.3067	0.0482	0.2571	0.0014	0.8085	0.8175
0.12	7.8	0.3091	0.0488	0.2574	0.0029	0.7943	0.8063
0.24	7.8	0.3129	0.0496	0.2576	0.0057	0.7664	0.7827
0.48	7.8	0.3197	0.0513	0.2567	0.0117	0.7030	0.7257

missions *WMAP* 9 and *Planck* 2015, using the six-parameter standard Λ CDM model. McCarthy et al. (2018) generated a suite of cosmological simulations that vary the baryonic physics model, the summed mass of neutrinos, and the background cosmology.

To explore the role of baryonic physics, we use the collisionless dynamics (DMONLY) run, the fiducial calibrated baryonic physics model (i.e. the model has been calibrated to reproduce the baryon fractions of groups and clusters), as well as two variations of the baryonic physics model where the efficiency of feedback from AGNs was raised (AGN high) and lowered (AGN low) to approximately bracket the observed baryon fractions of groups and clusters.

For the summed mass of neutrinos, McCarthy et al. (2018) ran simulations with $M_\nu = 0.06, 0.12, 0.24,$ and 0.48 eV . This was done both in the context of WMAP9 and Planck 2015 cosmologies (see McCarthy et al. 2018, for details). The present-day neutrino density of each run is $\Omega_\nu = \frac{\rho_\nu^0}{\rho_c^0} = M_\nu/(93.14 \text{ eV } h^2)$, using the present-day number density of neutrinos given by Lesgourgues & Pastor (2012), where ρ_ν and ρ_c^0 are the neutrino and critical densities today. When massive neutrinos were added in the *WMAP* 9-based cosmology, the cold dark matter density was reduced in order to keep a flat geometry, or $\Omega_b + \Omega_{\text{cdm}} + \Omega_\nu + \Omega_\Lambda = 1$. For the ‘*Planck* 2015/ A_{Lens} -based’ simulations used in this paper, the Markov Chains of Planck Collaboration XIII (2016a) corresponding to the ‘CMB+BAO + CMB lensing’ with marginalization over A_{Lens} (the amplitude of the CMB lensing power spectrum) was used (see fig. 2 of McCarthy et al. 2018). Cosmological parameter sets were selected that have summed neutrino mass within $\Delta M_\nu = 0.02 \text{ eV}$ of the target value, and the weighted mean of the other important cosmological parameters is taken from the Markov Chains. By selecting parameter values in this way, it ensures that the selected cosmologies are consistent with the CMB + BAO constraints and again preserving flatness, i.e. $\Omega_K = 0$. Note that there is an underlying fiducial baryonic physics for every model with non-zero M_ν . The details of the different runs are presented in Table 1.

3.2 Light-cones and synthetic lensing catalogues

The simulation boxes of BAHAMAS are $400 \text{ Mpc } h^{-1}$ per comoving side with each box containing 2×1024^3 particles. In order to construct BAHAMAS light-cones, McCarthy et al. (2018) saved particle data at snapshots from $z = 3$ to today. There are 15 snapshots at $z = 0.0, 0.125, 0.25, 0.375, 0.5, 0.75, 1.0, 1.25, 1.5, 1.75, 2.0, 2.25, 2.5, 2.75,$ and 3.0 . The snapshots were then randomly oriented and translated, and slices of $5 \times 5 \text{ deg}^2$ (at pixel resolution of 10 arcsec) were taken from the snapshots. A total of 25 randomizations of rotations and translations of the 15 snapshots were performed, the same for each cosmology and prescription for baryonic physics and neutrino mass, so that cosmic variance does not play a role when comparing light-cones across different runs. Here we consider 25 light-cones with a total area of 625 deg^2 .

The light-cones extracted from the simulations then give us ideal convergence maps, following Section 2, integrating the spatial matter overdensities $\delta(\chi, \theta)$ through the discrete slices along the line of sight with the kernel containing the source redshift distribution $p_s(z)$, as in equations (1) and (2). We adopt two different redshift distributions, one for the 450 deg^2 Kilo Degree Survey (KiDS-450; Hildebrandt et al. 2017) and one predicted for the LSST survey (Chang et al. 2013). The convergence maps for the former were created by McCarthy et al. (2018) and the convergence maps for the latter were constructed for this paper. Shear maps, and reduced shear maps, are constructed from convergence maps using equations (3) and (4). Synthetic catalogues of weakly lensed galaxies are generated using the reduced shear maps from the simulations.

We populate the maps with unlensed galaxies that are randomly placed on the sky, with number density appropriate for observations with a particular survey. The moduli of the complex ellipticities (related to the axial ratios) are drawn from a Gaussian distribution with $\sigma_{|\epsilon^s|} = 0.25$ and zero mean. Note that this value of 0.25 is for the modulus of ϵ^s rather than per component, hence the value is slightly lower than measured in observations (see e.g. fig. A3 of Schrabback et al. 2018). The galaxy orientation angles, ϕ^s , are

randomly assigned between 0 and π . At the position of a source galaxy, the reduced shear is extracted at the nearest pixel of the BAHAMAS maps. The observed ellipticity is determined using equation (6).

In this paper we roughly base one of the 625 deg² synthetic surveys on Hildebrandt et al. (2017), where they analyse ~ 450 deg² of imaging data from KiDS. In KiDS the effective number density of galaxies is 8.53 gal arcmin⁻² (the number density of galaxies was determined in Hildebrandt et al. 2017 by using the method proposed by Heymans et al. 2012), and the observed ellipticity dispersion is $\sigma_\epsilon \approx 0.29$ per component. For our first synthetic survey we use an effective source number density of 9 gal arcmin⁻².

We also consider synthetic surveys of the same 625 deg² area, but with convergence (shear and reduced shear) maps constructed using the source redshift distribution from Chang et al. (2013), estimated for the deeper upcoming LSST. Both LSST and *Euclid* (Laureijs et al. 2011; Amendola et al. 2018) surveys have an expected effective galaxy source number density $n_{\text{eff}} = 30$ gal arcmin⁻². We also consider $n_{\text{eff}} = 60$ gal arcmin⁻² when we create our synthetic lensing catalogues, to reflect deeper space-based characteristics, such as the *HST* (see for example the source number density in King et al. 2016). Note that we use the same redshift distribution for this even deeper survey, but increase the effective number density of sources from which the shear can be measured. This neglects the contribution from some higher redshift galaxies which carry a more significant lensing signal than lower redshift ones. The different surveys with the effective number density of 9, 30, and 60 gal arcmin⁻² will be referred to as KiDS, Deep Ground Based or Space Based (DGB/SB), and Deep Space Based (DSB), respectively.

Similar to Martinet et al. (2018), on the 625 deg² we generate five synthetic catalogues of source ellipticities at the same positions but with random shapes per suite (as in Table 1) to make sure that the simulations are not biased to one particular realization of shape noise.

4 APERTURE MASS PEAKS

In this section we outline the aperture mass statistic (Schneider 1996) that we use to measure the WL signal, and how we map the aperture mass over the synthetic surveys. Finally we describe how we determine the WL peaks based on the aperture mass maps.

4.1 Aperture mass statistic

We can take advantage of the fact that the average shape of unlensed galaxies is circular for a large enough sample, or $\langle \epsilon^s \rangle = 0$. So if we take an ensemble of lensed galaxy shapes over a small patch of sky, we can recover the reduced shear, $\langle \epsilon \rangle = g$ (see equation 6).

An important tool is the aperture mass (Schneider 1996), which can be used to map dark and luminous matter. Although not employed in this paper, the variance of the aperture mass as a function of aperture scale can be used to constrain cosmological parameters using cosmic shear (e.g. see Schneider 2005, and references therein). The aperture mass statistic has been used on wide field surveys to identify massive objects, e.g. Hettterscheidt et al. (2005). Various cluster detection methods that incorporate tomographic redshift information for the source galaxies and different shapes of filter function have also been developed (e.g. Schirmer et al. 2007; Maturi et al. 2010). For example, Hennawi & Spergel (2005) considered the efficiency of cluster detection using the aperture mass statistic and also including tomographic information and optimal filtering.

The aperture mass, M_{ap} , is constructed by integrating the weighted convergence within an aperture:

$$M_{\text{ap}}(\vec{\theta}_0) = \int d^2\theta U(\vec{\theta} - \vec{\theta}_0) \kappa(\vec{\theta}), \quad (7)$$

where θ_0 is the 2D location of the aperture centre, and U is a weight function that is compensated within the filter radius, smoothly goes to zero at a finite radius, and is zero outside of that radius. It should also be localized in Fourier space with no oscillatory behaviour in the power spectrum (Leonard, Pires & Starck 2012). Since the convergence and the shear are related (see Section 2), the aperture mass can be expressed as

$$M_{\text{ap}}(\vec{\theta}_0) = \int d^2\theta Q(\vec{\theta} - \vec{\theta}_0) \gamma_t(\vec{\theta}, \vec{\theta}_0), \quad (8)$$

where the shear weight function or filter function is $Q(\theta) = \frac{2}{\theta^2} \int_0^\theta d\theta' U(\theta') - U(\theta)$ and the tangential shear is $\gamma_t \approx g_t$ in the WL limit.

In practice for real or synthetic observations of lensed galaxies we express the integral in equation (8) as a sum over discrete galaxies. The aperture mass then becomes the weighted sum over the tangential ellipticities:

$$M_{\text{ap}}(\vec{\theta}_0) = \frac{1}{n_{\text{gal}}} \sum_i^{N_{\text{gal}}} Q(\vec{\theta}_i - \vec{\theta}_0) \epsilon_t(\vec{\theta}_i, \vec{\theta}_0), \quad (9)$$

where n_{gal} is the number density of observed galaxies inside the aperture, N_{gal} is the total number of galaxies inside the aperture, and ϵ_t is the observed tangential ellipticity of a galaxy expressed as

$$\epsilon_t(\vec{\theta}, \vec{\theta}_0) = -[\epsilon_1(\vec{\theta}) \cos(2\varphi(\vec{\theta}, \vec{\theta}_0)) + \epsilon_2(\vec{\theta}) \sin(2\varphi(\vec{\theta}, \vec{\theta}_0))], \quad (10)$$

where $\varphi(\vec{\theta}, \vec{\theta}_0)$ is the angular position with respect to the centre of the aperture.

Filter functions are optimized for different applications (see for example Maturi et al. 2010). In this work we use a filter function that is optimized to detect NFW haloes taken from Schirmer et al. (2007):

$$Q_{\text{NFW}}(x) = \frac{1}{1 + e^{6-150x} + e^{-47+50x}} \frac{\tanh(x/x_c)}{x/x_c}, \quad (11)$$

where $x = \theta/\theta_{\text{ap}}$ is the angular distance from the aperture centre θ_0 scaled by the filter size θ_{ap} . x_c is analogous to the halo concentration in the NFW profile, and it was empirically set to $x_c = 0.15$ in Hettterscheidt et al. (2005). This is consistent with Martinet et al. (2018). Fig. 1 is a plot of the filter function, $Q_{\text{NFW}}(x)$ (equation 11), used in this work. Note that the filter function down-weights galaxies towards the centre of the aperture, which excludes contamination by the presence of a bright central galaxy in a cluster and the strong lensing regime. Furthermore there is a possibility that the impact of different baryonic physics models can be mitigated due to the down-weight or exclusion of the central region in the filter. Compared to DMONLY, free-streaming neutrinos suppress the median halo density profile roughly independent of the distance to the centre, while baryonic physics effects depend more strongly on the distance (see Mummery et al. 2017). The filter function is truncated at $\theta = \theta_{\text{ap}}$ and the aperture mass is calculated within the filter size, θ_{ap} .

4.2 S/N peaks

To calculate the S/N ratio for the aperture mass statistic we proceed as in Martinet et al. (2018), where the standard deviation of the

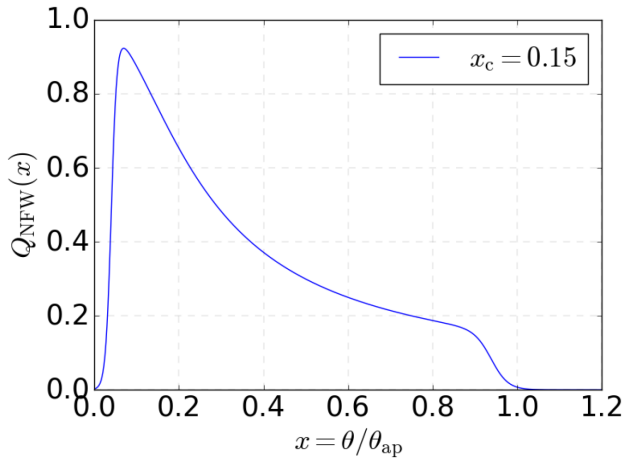


Figure 1. $Q_{\text{NFW}}(x)$ is the aperture mass filter function used in this work (equation 11), taken from Schirmer et al. (2007). The aperture mass calculated in equation (9) cuts off at the filter size, $\theta = \theta_{\text{ap}}$ and the falloff towards the centre would down-weight a bright central galaxy in a galaxy cluster and the strong lensing regime.

aperture mass in the absence of shear is given by

$$\sigma(M_{\text{ap}}(\bar{\theta}_0)) = \frac{1}{\sqrt{2n_{\text{gal}}}} \left(\sum_i^{N_{\text{gal}}} |\epsilon(\bar{\theta}_i)|^2 Q^2(\bar{\theta}_i - \bar{\theta}_0) \right)^{\frac{1}{2}}. \quad (12)$$

The S/N ratio for an aperture measurement is given by

$$\frac{S}{N}(\bar{\theta}_0) = \frac{\sqrt{2} \sum_i^{N_{\text{gal}}} Q(\bar{\theta}_i - \bar{\theta}_0) \epsilon_i(\bar{\theta}_i, \bar{\theta}_0)}{\sqrt{\sum_i^{N_{\text{gal}}} |\epsilon(\bar{\theta}_i)|^2 Q^2(\bar{\theta}_i - \bar{\theta}_0)}}. \quad (13)$$

We use publicly available software, developed by Bard et al. (2013), which implements GPU computing for fast calculation of the aperture mass. This algorithm uses the positions and shapes of galaxies in this calculation. For a compromise between computational efficiency and optimized resolution for peak detection, the grid resolution of the aperture maps (where the apertures are centred) is set to 512×512 pixels which is 0.5859 arcmin per pixel, similar to Martinet et al. (2018). The algorithm scans the grid points over the synthetic WL catalogues and returns the aperture mass, variance, and S/N values. We ran the code on the synthetic data from Section 3.2 using filter sizes $\theta_{\text{ap}} = 8.0, 10.0, 12.5,$ and 15.0 arcmin. Fig. 2 shows a sample of the direct overlay of the S/N contours (lower limit of S/N at 0 and contours increase in increments of 1) on top of the BAHAMAS light-cone convergence map (grey scale) which is produced by integrating the weighted line-of-sight overdensities according to equation (1). The cross marks are the locations of galaxy clusters taken directly from the BAHAMAS friends-of-friends (FoF) catalogues. The triangles are the S/N peak locations ($S/N > 2$) obtained by a peak detection PYTHON script which examines if each pixel of the S/N map has a higher value than the eight nearest neighbouring pixels. We focus on the analysis of the statistics of these peaks in our work.

To quantify the difference in the WL peak counts for varying survey characteristics, and for simulation runs with different baryonic physics and summed neutrino mass, we take the ratio of the WL peak distributions with respect to the reference models. We use five different shape noise realizations for each simulation run, consistent with Martinet et al. (2018), in order to avoid potential bias to one particular noise realization. Varying only shape noise

neglects sample variance which is partially accounted for by using several different line of sights through the simulations, in that we use 25 light-cones.

Note that Martinet et al. (2018) used dark matter only simulations to investigate the impact of a much wider range of cosmologies (particularly considering Ω_m and σ_8) on peak counts for comparison with KiDS data. In this work, as noted in the introduction, we focus on investigating the impact of baryonic processes (including star formation, AGN feedback, and supernova feedback) and massive neutrinos on the peak statistics.

5 RESULTS

In Section 5.1 we present the results of our studies on the impact of baryonic physics and summed neutrino mass on the WL peak statistics. Then in Section 5.2 we present the results on how summed neutrino mass affects the correlation between higher S/N peaks and massive clusters. In both subsections we consider synthetic surveys with different source redshift distributions and effective number density of sources from which lensing shear can be measured. These synthetic surveys are referred to as KiDS, DGB/SB, and DSB, as outlined in Section 3.2.

5.1 Dependence of weak lensing peak counts on baryonic physics and summed neutrino mass

Figs 3 and 4 show the impact of the different baryonic physics models and summed neutrino mass in *WMAP* 9 and *Planck* 2015 cosmologies for the KiDS and DGB/SB survey, respectively. The filter size is fixed at 12.5 arcmin for consistency with Martinet et al. (2018). In the top panels of each subfigure the S/N peak distributions are presented, and the bottom panels show the ratio of the distributions with respect to the reference model. Note that the bins are spaced linearly in S/N from 0 to 5 in 13 bins, with the markers indicating the bin centres.

Figs 3(a) and 4(a) show the impact of baryonic processes on the WL peak statistics with different background source number densities of 9 and 30 gal arcmin⁻², respectively. The bottom panels show the ratio of the S/N distributions for different AGN feedback strengths with respect to the DMONLY case. Note that in this case massive neutrinos are not included. In Fig. 3(a), with $n_{\text{eff}} = 9$ gal arcmin⁻², the low S/N peaks show a modest boost from baryons resulting in only a few per cent deviation from DMONLY. However in Fig. 4(a), with $n_{\text{eff}} = 9$ gal arcmin⁻², the low S/N peak counts tend to be boosted by up to about 6 per cent in comparison with DMONLY. According to the discussion in Martinet et al. (2018), much of the constraining power of peak counts for cosmological models comes from the lower S/N range. Our results indicate that when baryonic processes are accounted for in the error budget, care should be taken to calibrate the impact of baryons as a function of the source number density. Effects of different aperture filter sizes on the S/N distributions is discussed in Section 5.2 and more specific examples are shown in the online Appendix Figs A1–A6.

In DMONLY simulations higher S/N peak values are more likely to be produced by more massive clusters, although there is an additional complication due to the dependence of peak height on cluster redshift for a given source population (e.g. fig. 17 of Hamana, Takada & Yoshida 2004). The impact of baryons is more significant at higher S/N, where higher peak values are more likely to arise from massive haloes (Hennawi & Spergel 2005). The massive haloes are more likely to have greater AGN feedback strength that cause the mass density profiles to be flatter and less concentrated

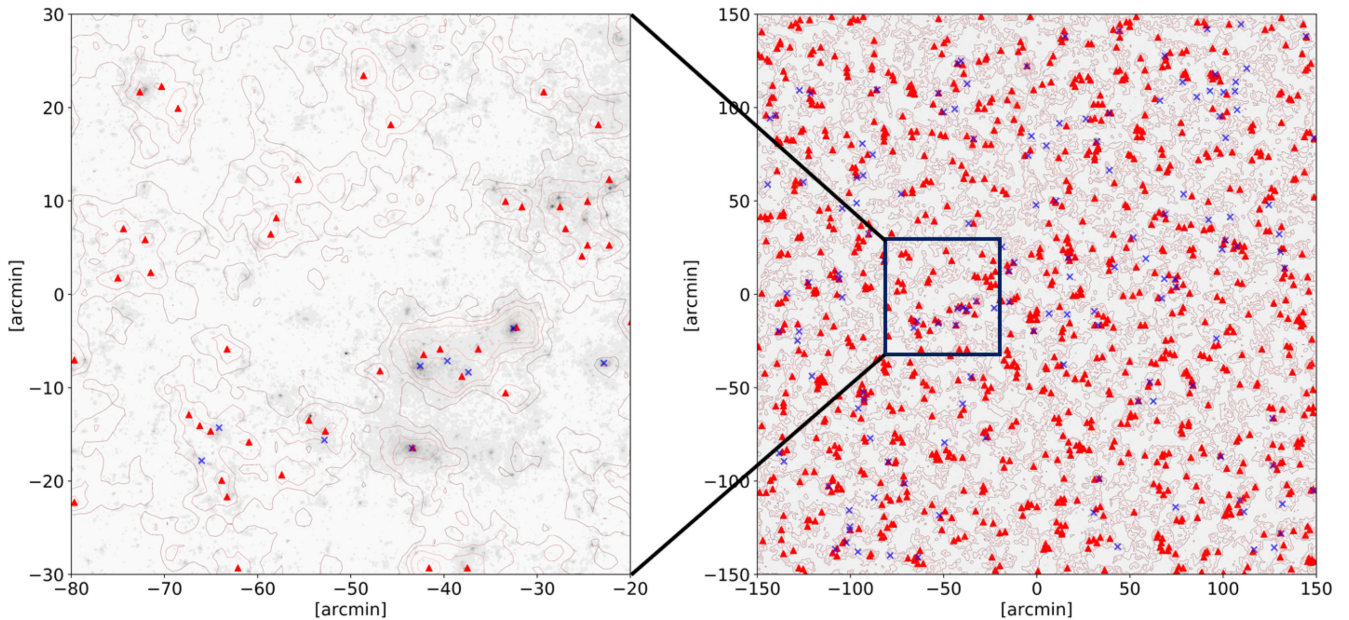


Figure 2. A 60×60 arcmin² subregion of a 5×5 deg² aperture mass map for source number density $9 \text{ gal arcmin}^{-2}$. The aperture size is 12.5 arcmin, and the S/N contour lines are plotted from 0 with an increment of 1. The field in grey scale in the background is the light-cone convergence map, and the cross marks are the locations of clusters from the BAHAMAS FOF catalogues, where the lowest mass cut is $10^{14} M_{\odot}$ and the upper limit redshift cut for the clusters is at $z = 0.5$. The triangles are the peak locations above $S/N = 2$.

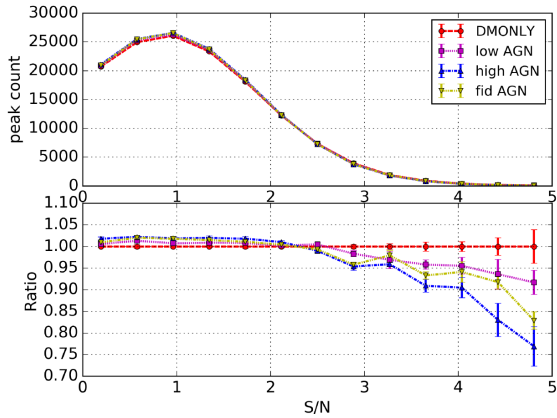
(Mummery et al. 2017), thereby returning lower S/N values than the DMONLY case and having a larger effect on the high S/N peaks. In Table 1 the S_8 values do not vary with AGN temperature, yet these plots show that increasing AGN temperature changes the peak distribution similar to decreasing S_8 (see Martinet et al. 2018). In agreement with previous work (e.g. Osato et al. 2015), this implies that estimating cosmological parameters when using cosmological simulations without baryonic processes can lead to a bias. This is also true for the summed neutrino mass, as discussed below. Additionally, the deviation among the higher S/N peak counts with different AGN feedback strength is hard to resolve, even though the error bars due to scatter from the different shape noise realizations are tighter than those for the lower number density of sources (as anticipated).

The middle panels, Figs 3(b) and 4(b) (9 and 30 gal arcmin⁻², respectively), are the S/N peak distributions for different summed neutrino mass. Note that all models here include the underlying fiducial baryonic physics prescription. The S/N peak counts show that there is a negative (positive) difference for the higher (lower) S/N peaks for all of the M_{ν} models (with the exception of the last S/N peak bin in the 0.06 eV model, where the statistics in this bin are poor). Furthermore increasing M_{ν} suppresses (boosts) the higher (lower) S/N peaks. This is expected as free-streaming neutrinos impede the growth of LSS and therefore have a larger impact on more massive haloes, suppressing the high end of the halo mass function more significantly with increasing neutrino mass (e.g. Costanzi et al. 2013; Mummery et al. 2017).

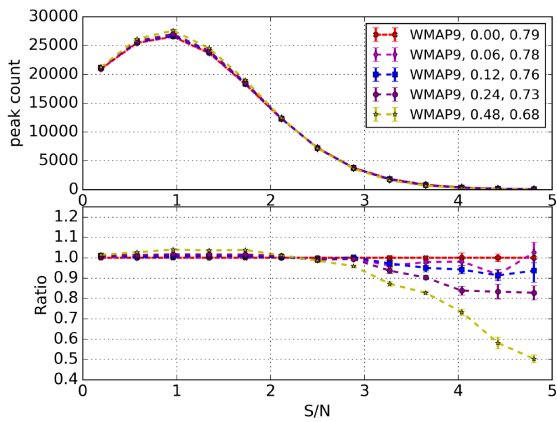
Note the similarity of the suppression (boosting) in high (low) S/N peak counts due to AGN feedback and massive neutrinos. This can make differentiating baryonic physics and massive neutrinos based purely on S/N peak counts quite difficult. Mummery et al. (2017) shows that baryonic physics and summed neutrino mass impact on the halo mass function and halo clustering and matter clustering (or matter power spectrum, $P(k)$), independently. That

is, the separate effects of baryonic physics and summed neutrino mass can be multiplied to estimate the combined effect within a few per cent error. Since the WL peak statistics depends on the mass function and on the convergence (equation 7), the S/N peak counts should behave similarly. Furthermore, because baryonic physics and summed neutrino mass alter the halo mass function and matter clustering with a different dependence on redshift (see Figs 1 and 13 of Mummery et al. 2017), this can potentially be used to distinguish and quantify the effects when considering S/N peak counts in tomographic redshift bins. The redshift dependence of the peak counts could be explored within the framework of the halo model using modifications to haloes to account for baryonic physics and modelling the impact on their formation histories as a result of massive neutrinos (e.g. Hamana et al. 2004; Semboloni et al. 2011; Massara, Villaescusa-Navarro & Viel 2014; Mead et al. 2016). Another possibility is to harness the differential impact of baryonic physics and massive neutrinos on halo mass density profiles, as shown in Mummery et al. (2017). Choosing different filter shapes and sizes should then have an impact on the detection of peaks as a function of baryonic physics and massive neutrinos. For example, the optimization of S/N for specific objects depends on the filter and its parameters. In this work we use a filter optimized for NFW haloes (equation 11 as given by Schirmer et al. 2007). Filters can also be adjusted to better study haloes of particular masses and redshifts (see e.g. Hettterscheidt et al. 2005). A detailed treatment of these topics is beyond the scope of this paper and will be considered in future work.

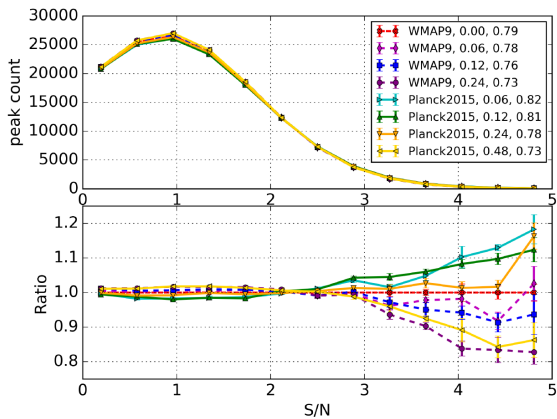
The impact of *WMAP* 9 and *Planck* 2015 cosmologies for $M_{\nu} = 0.00, 0.06, 0.12, 0.24,$ and 0.48 eV summed neutrino mass models (all with fiducial baryonic physics) are compared with *WMAP* 9 $M_{\nu} = 0.00$ eV, as a reference model, in Figs 3(c) and 4(c), for 9 and 30 gal arcmin⁻², respectively. Note that we exclude the *WMAP* 9 $M_{\nu} = 0.48$ eV model as it is well outside of the range of the *Planck* 2015 models (see Figs 3b and 4b). The peak counts



(a)

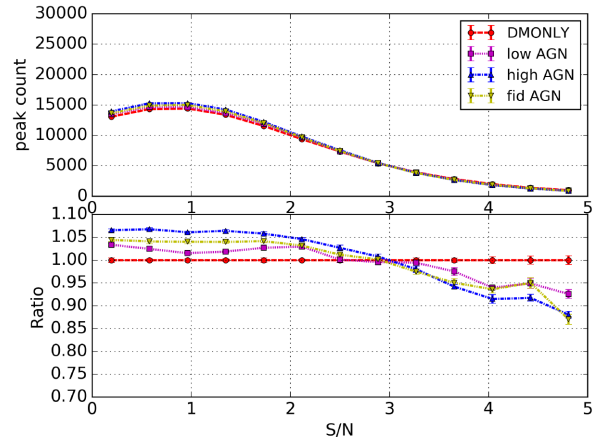


(b)

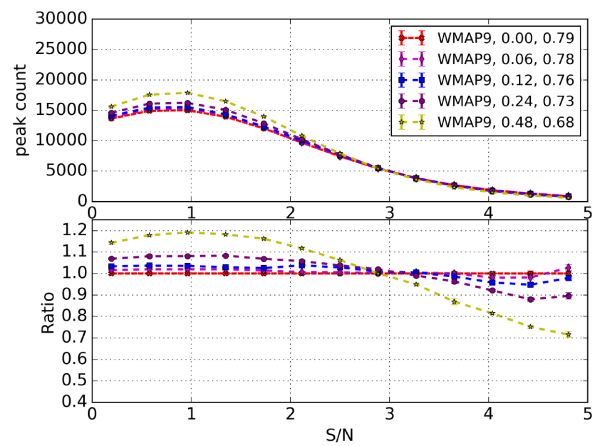


(c)

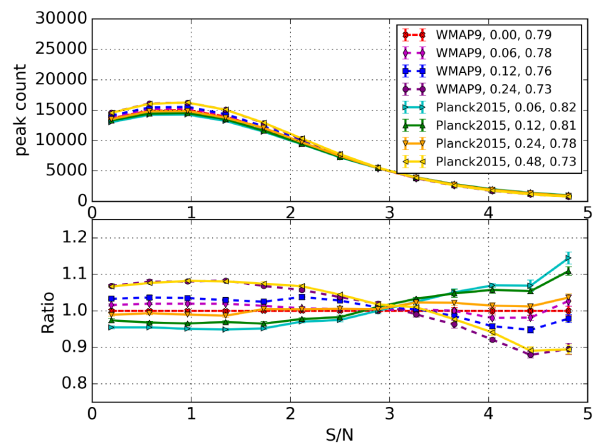
Figure 3. The impact of (a) baryonic physics, (b) massive neutrinos, and (c) *WMAP* 9 and *Planck* 2015 cosmologies on the WL peak statistics with aperture filter size of 12.5 arcmin^{-2} . The bottom panels show the ratio, taking the ratio with the *WMAP* 9 DMONLY results for subplot (a) and *WMAP* 9 with fiducial AGN feedback for subplots (b) and (c). Note that we exclude the *WMAP* 9 $M_\nu = 0.48 \text{ eV}$ model in (c) as it is well outside of the range of the *Planck* 2015 models. All of the models in (b) and (c) have fiducial baryonic physics. The error bars show the variance of the five different shape noise realizations. In (b) and (c) the legend entries are Cosmology, M_ν (eV), and S_8 . Note that the bins are spaced linearly in S/N from 0 to 5 in 13 bins with the markers indicating the bin centres.



(a)



(b)



(c)

Figure 4. Comparison of the WL peak distributions with the higher source number density ($30 \text{ gal arcmin}^{-2}$) for DGB/SB surveys. The other parameters such as the intrinsic ellipticity dispersion and the suites of simulations are the same as in Fig. 3. Note that we exclude the *WMAP* 9 $M_\nu = 0.48 \text{ eV}$ model in (c) as it is well outside of the range of the *Planck* 2015 models. All of the models in (b) and (c) have fiducial baryonic physics. The error bars show the variance of the five different shape noise realizations. In (b) and (c) the legend entries are Cosmology, M_ν (eV), and S_8 . Note that the bins are spaced linearly in S/N with the markers indicating the bin centres.

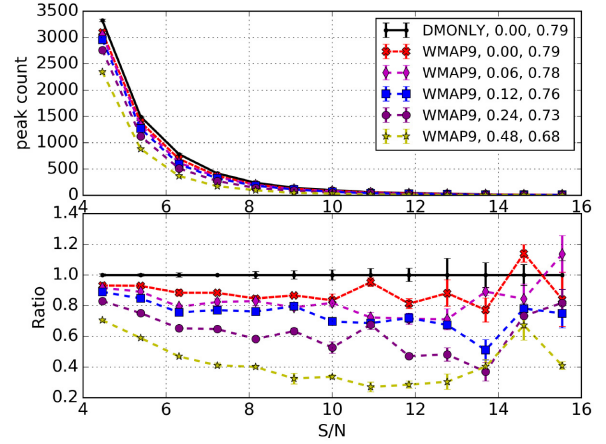
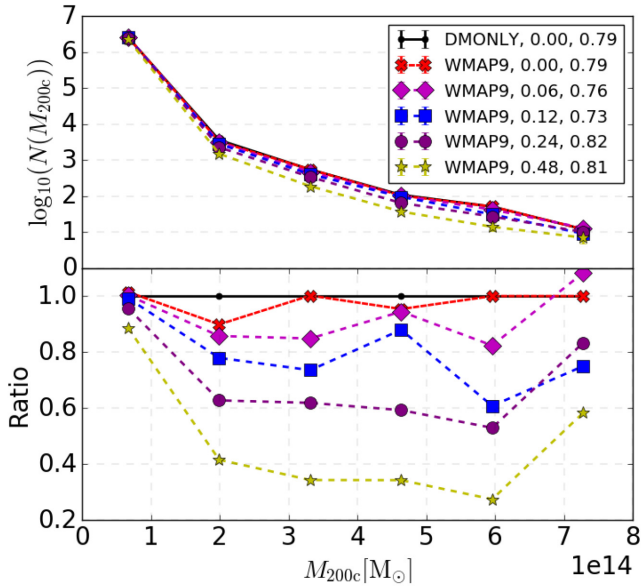


Figure 5. Impact of summed neutrino mass with underlying fiducial baryonic physics ($M_\nu = 0.00, 0.06, 0.12, 0.24,$ and 0.48 eV models, all with fiducial baryonic physics, see Table 1). The left-hand panel shows the halo mass function (plotted for redshifts out to $z = 0.9$) and the right-hand panel shows the S/N peak count distributions, compared with the DMONLY model (collisionless dynamics). This is shown for the DGB/SB (30 gal arcmin $^{-2}$) survey based on WMAP 9 cosmology. The legend is labelled as Cosmology, M_ν (eV), and S_8 . The comparisons in the bottom panels are with respect to the DMONLY (collisionless dynamics) model. The error bars show the estimated error using Poisson noise ($\sqrt{N(M_{200c})}$) on the left-hand panel and the variance of the five different shape noise realizations on the right-hand panel. In the figures we extend the S/N from 4 to 16 in 13 bins in order to assess the impact on very high S/N peaks, which are more likely produced by higher mass haloes.

with the *Planck* 2015 cosmology for the M_ν 0.06–0.24 eV models also show a positive (negative) difference for the higher (lower) S/N peaks, with respect to the WMAP 9 $M_\nu = 0.00$ eV reference model. Furthermore the *Planck* 2015 $M_\nu = 0.24$ and 0.48 eV models clearly bracket the WMAP 9 $M_\nu = 0.00, 0.06,$ and 0.12 eV models for both KiDS and DGB/SB. This suggests degeneracy between summed neutrino mass and other cosmological parameters in the framework of fiducial baryonic physics. Importantly the S/N peak counts are roughly ordered with respect to the S_8 values ($S_8 = \sigma_8 \sqrt{\Omega_m}/0.3$, see Table 1), in agreement with Martinet et al. (2018). The BAHAMAS simulations were carried out with initial amplitude of density fluctuations normalized to the CMB, rather than normalized to have the same σ_8 today. However, using simulations with massive neutrinos and dark matter, Costanzi et al. (2013) found that when simulations were normalized to have the same σ_8 today (with the same value of Ω_m), even for a very high value of summed neutrino mass the halo mass function is very close to that of a dark matter only simulation, out to $z = 1$.

For DGB/SB the WL peak counts with $M_\nu = 0.12$ eV for WMAP 9 and *Planck* 2015 have an absolute maximum relative difference of ~ 5 and ~ 10 percent, respectively (up to S/N of 5), compared with the WMAP 9 zero neutrino mass model. As can be seen from Fig. 4(c), the differences between the peak counts for suites with summed neutrino masses 0.06 and 0.12 eV inside the WMAP 9 and *Planck* 2015 cosmologies are smaller than the differences between the counts across the cosmologies. However for higher summed neutrino mass, models across cosmologies but with similar S_8 values have peak counts that are difficult to distinguish. For example the WMAP 9 $M_\nu = 0.00$ (0.24) eV model has similar peak counts to the *Planck* 2015 $M_\nu = 0.24$ (0.48) eV model.

Fig. 1 in Mummery et al. (2017) shows that the halo mass function is well represented by a product of the separate impacts

of baryonic physics (even with extreme AGN feedback strengths) and summed neutrino mass. The figure shows that the baryonic physics prescription has a larger impact in the 10^{13} – 10^{14} M_\odot range, but becomes more like DMONLY for the high-mass range. That is because the AGN feedback ejects matter from the centre of galaxy clusters, but as the cluster mass becomes larger the ejected matter is more likely to stay bound with the cluster. The figure also shows that increasing summed neutrino mass tends to suppress the halo mass function, with greater effect for higher mass bins. The combined effects can be seen in the left-hand panel of Fig. 5 (plotted for redshifts out to $z = 0.9^2$). The error bars are estimated with the Poisson noise ($\sqrt{N(M_{200c})}$). Note that the error bars are small. The impact of summed neutrino mass, all with fiducial baryonic physics, on the halo mass function is compared with the DMONLY model (collisionless dynamics). As the summed neutrino mass increases, the halo mass function becomes further suppressed towards the middle of the distribution. But the distribution is more similar to DMONLY for higher mass bins. This reflects the independent behaviour described in Mummery et al. (2017), where the separate impacts are multiplicative.

In the right-hand panel of Fig. 5 we show how summed neutrino mass with fiducial baryonic physics impacts on the S/N peaks, over a wide range of S/N values. In the figures we extend the S/N from 4 to 16 in 13 bins in order to assess the impact on very high S/N peaks. The high S/N values are more likely produced by massive clusters and should reflect the behaviour seen in the halo mass function (left-hand panel of Fig. 5). This shows how increasing summed neutrino mass with fiducial baryonic physics suppresses the S/N peaks, but

²The distribution amplitudes grew for higher redshift ranges, but the ratios remained mostly the same.

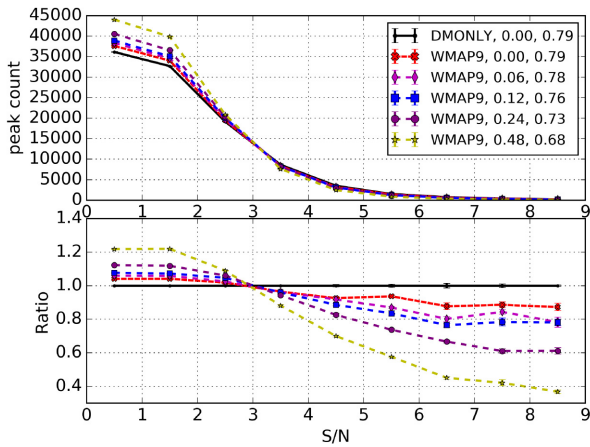
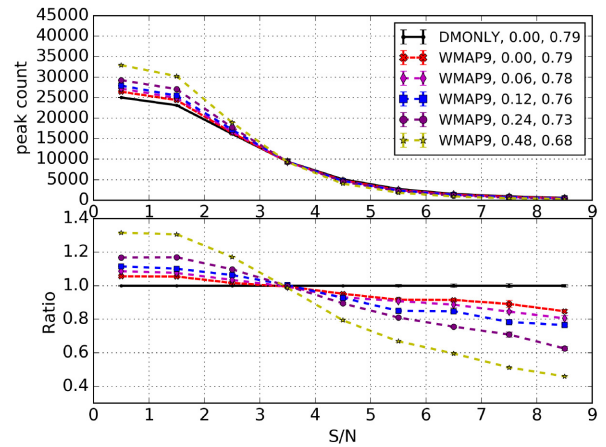

 (a) 30 gal/arcmin²

 (b) 60 gal/arcmin²

Figure 6. Impact of baryonic physics and neutrino mass, $M_\nu = 0.00, 0.06, 0.12, 0.24,$ and 0.48 eV models, all with fiducial baryonic physics, on the S/N peak distributions from DGB/SB (30 gal arcmin⁻²) and DSB (60 gal arcmin⁻²) surveys based on *WMAP* 9 cosmology. The legend goes as Cosmology, M_ν (eV), and S_8 . The comparisons in the bottom panels are with respect to the DMONLY (collisionless dynamics) model with zero neutrino mass. The error bars show the variance of the five different shape noise realizations. In this figure we extend the S/N from 0 to 10 in nine bins in order to assess the impact at high S/N. Note that the amplitudes of the peak counts are different from Figs 3(b) and 4(b) due to wider binning.

the peak counts turn over and tends toward DMONLY for the higher S/N bins. This can be explained by the combined impact of baryonic physics and summed neutrino mass on the halo mass function. Note that the amplitudes of the peak counts are different from Fig. 4(b) due to wider binning and that the bins are spaced linearly in S/N with the markers indicating the bin centres.

Fig. 6 illustrates how the numbers of the peak counts change with source number densities of 30 and 60 gal arcmin⁻², DGB/SB and DSB survey WL characteristics, respectively (both use the same redshift distribution when constructing the lensing convergence). In this figure we extend the S/N from 0 to 10 in nine bins, with the markers indicating the bin centres, in order to assess the impact at high S/N. Note that the amplitudes of the peak counts are different from Figs 3(b) and 4(b) due to wider binning. The peak counts of these models are compared with those of DMONLY. Higher source number density tends to offset the impact of shape noise, suppressing the number of lower S/N peak counts and boosting the higher S/N peak counts, while also decreasing the scatter in peak counts from field to field. This can be explained by generating a shape-noise-only field, where the field of view is populated by galaxies with ellipticities drawn from a Gaussian distribution (with appropriate number density) and with no foreground structure (as in the noise-only fields in Martinet et al. 2018). Adding real foreground structure from the light-cones increases (decreases) the number of higher (lower) S/N values. Our results highlight that accounting for the impact of baryonic physics and massive neutrinos in observational surveys must take the source number density into consideration. Furthermore a given real structure is more likely to have a higher corresponding S/N value with increasing source number density. We discuss this further in Section 5.2.

Fig. 7 (corresponding values listed in Table 2) compares the peak counts in *WMAP* 9 $M_\nu = 0.0, 0.06, 0.12, 0.24,$ and 0.48 eV models (all with fiducial baryonic physics) to DMONLY, for DGB/SB data. Assuming that baryonic physics and massive neutrinos act independently (Mummery et al. 2017): at lower summed neutrino mass, 0.06 and 0.12 eV, the impact of fiducial baryonic physics on the peak counts tends to be greater than that of massive neutrinos

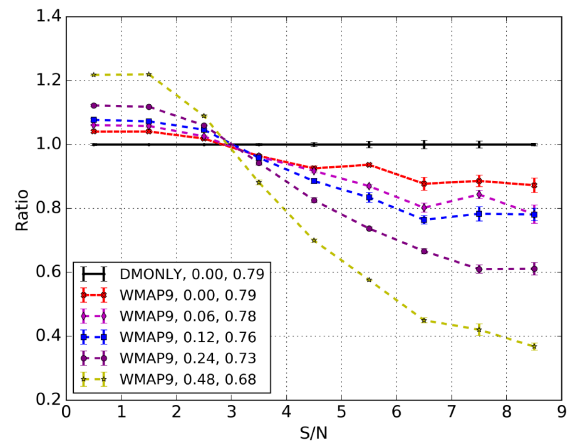


Figure 7. Relative percentage differences in peak counts with respect to the DMONLY peak count distribution (Fig. 6a). For the DGB/SB survey, five models ($M_\nu = 0.00, 0.06, 0.12, 0.24,$ and 0.48 eV, all with fiducial baryonic physics) of the *WMAP* 9 cosmology are compared with the DMONLY model in order to determine percentage differences in each interval of S/N. The legend is labelled as Cosmology, M_ν (eV), and S_8 .

up to S/N ~ 5 ; at higher summed neutrino mass, 0.24 and 0.48 eV, the presence of massive neutrinos tends to be more important than fiducial baryonic physics. These conclusions are also sensitive to the source number density and intrinsic galaxy ellipticity dispersion.

5.2 Results on high S/N weak lensing peaks

In the previous subsection we compared our results to the DMONLY model for consistency with Mummery et al. (2017), where it was shown that baryons and neutrinos impact on the halo mass function independently and that their effects are multiplicative. In this subsection we focus on the high S/N peaks for the *Planck* 2015 cosmology with fiducial baryonic physics and varying neutrino

Table 2. The relative percentage differences in S/N peak counts for the DGB/SB survey (these values are taken from Figs 6a and 7). The values are in units of per cent and compare the five different simulations ($M_\nu = 0.0, 0.06, 0.12, 0.24,$ and 0.48 eV, all with fiducial baryonic physics) per S/N bin with the DMONLY simulation.

S/N	M_ν (eV)				
	0.00	0.06	0.12	0.24	0.48
0–1	4.1	6.1	7.7	12.2	21.8
1–2	4.1	5.8	7.3	11.9	22.0
2–3	1.9	2.6	4.6	6.0	9.0
3–4	−3.6	−3.8	−4.1	−5.7	−11.9
4–5	−7.4	−8.2	−11.4	−17.4	−30.0
5–6	−6.3	−13.0	−16.5	−26.3	−42.4
6–7	−12.3	−19.8	−23.5	−33.3	−53.0
7–8	−11.4	−15.6	−21.7	−39.0	−56.0
8–9	−12.7	−21.8	−21.9	−38.9	−63.2
9–10	−16.2	−15.4	−26.8	−42.3	−67.5

mass, where the implementation of neutrinos in the simulations impact on other cosmological parameters other than Ω_{cdm} . We discuss: (1) How summed neutrino mass affects the high-mass end of the halo mass function and also give some examples of the impact on the mass of specific clusters. (2) S/N peak dependence on survey characteristics and noise. (3) How filter size impacts the detection of high S/N peaks. (4) Using cluster positions to find nearby S/N peaks to study the correlation between cluster mass and S/N peaks. This would be analogous to targeting clusters (for example known clusters or clusters selected using another technique) and measuring their aperture mass signal. (5) Using S/N peak locations to find nearby clusters, analogous to carrying out a blind WL survey.

We use the FoF catalogues, containing halo information within the light-cones, from the simulation selecting objects with masses $M_{200c} \geq 10^{14} M_\odot$ and $z \leq 0.9$. Clusters are identified by running an FoF algorithm on the full simulation snapshot data. Spherical overdensity masses for the FoF groups are calculated using the SUBFIND algorithm. An overdensity of 200 with respect to the critical density at the snapshot redshift of the FoF group is used (i.e. M_{200c}).

In the top panel of the left-hand panel of Fig. 5 we plot the number counts of clusters for each neutrino mass suite for the *WMAP* 9 cosmology. For the bottom panel we take the ratios with respect to the $M_\nu = 0.06$ eV number counts. The left-hand panel of Fig. 5 shows that when the summed neutrino mass increases there are progressively fewer massive haloes of a particular mass. Comparing the number counts to the $M_\nu = 0.06$ eV model, the trends with increasing summed neutrino mass are similar for both *WMAP* 9 and *Planck* 2015 cosmologies (not plotted here). These results are consistent with the findings of e.g. Costanzi et al. (2013), Castorina et al. (2014), Mummery et al. (2017), and Hagstotz et al. (2019).

The reason for this trend is that neutrinos can free-stream out of overdense regions which inhibits the growth of structure. Increasing the mass in the neutrino component means that a larger fraction of the total mass can free-stream out. We also studied the impact of summed neutrino mass on cluster shapes by analysing their moment of inertia tensors, finding that their axial ratios have no significant change but the overall sizes are altered. This will be a subject of a future paper.

Fig. 8 shows the spatial distribution of massive clusters in a $1 \times 1 \text{ deg}^2$ field of view for four different simulations, where they only differ by neutrino mass. The four panels are $M_\nu = 0.06, 0.12,$

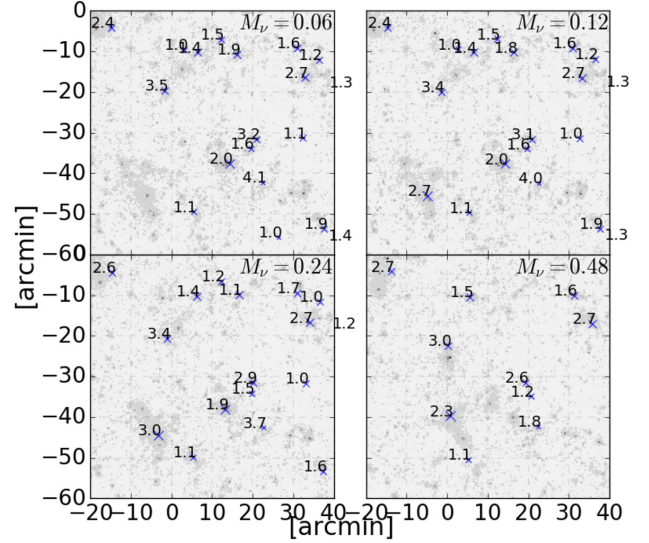


Figure 8. The locations of clusters on the convergence maps for different summed neutrino mass. This is the same field of view for four different simulations in the *Planck* 2015 cosmology with $n_{\text{eff}} = 9 \text{ gal arcmin}^{-2}$. The four panels have $M_\nu = 0.06, 0.12, 0.24,$ and 0.48 eV for the top left, top right, bottom left, and bottom right panels respectively. The grey scale is the convergence map and \times s are the cluster locations. The smaller the \times the higher the cluster redshift. The values next to the \times s are the cluster masses in units of $10^{14} M_\odot$.

0.24, and 0.48 eV for the top left, top right, bottom left, and bottom right panels, respectively. The grey scale is the convergence map and \times s are the cluster locations. The smaller the \times the higher the cluster's redshift. The values next to the \times s are the cluster masses in units of $10^{14} M_\odot$. This shows that with increasing summed neutrino mass most cluster masses decrease (see the left panel of Fig. 5), though not all. Note that we only show cluster masses $M_{200c} \geq 10^{14} M_\odot$, and some clusters drop below this limit.

5.2.1 Noise realizations

We study a total of five shape noise realizations of WL on 625 deg^2 , for the *Planck* 2015 cosmology with $M_\nu = 0.06$ eV. As described above, each noise realization has a different set of random seeds for intrinsic galaxy ellipticities (see Section 3.2). The galaxy positions are the same for each run. In this section we consider cluster-mass objects and high peak values ($S/N \geq 3$).

For KiDS (DGB/SB) data with $n_{\text{eff}} = 9$ (30) gal arcmin^{-2} , Fig. 9(a) (Fig. 9b) shows the impact of different shape noise realizations on the aperture mass maps and S/N peaks. Each panel shows the same $1 \times 1 \text{ deg}^2$ field of view. The grey scale and \times markers are the convergence maps and cluster locations respectively. The line contours and triangles are the aperture mass S/N and S/N peaks (≥ 3), respectively. A smaller triangle or \times corresponds to a lower S/N peak value or a higher cluster redshift, respectively. \times markers and the convergence maps do not change between noise realizations because they are taken directly from the BAHAMAS simulation. Figs 9(a) and (b) show that aperture mass S/N maps and therefore peak locations depend heavily on the noise realization, but are more consistent for a higher effective number density of source galaxies. The match between S/N peaks and cluster locations is in rough agreement with Hamana et al. (2004), Yang et al. (2011),

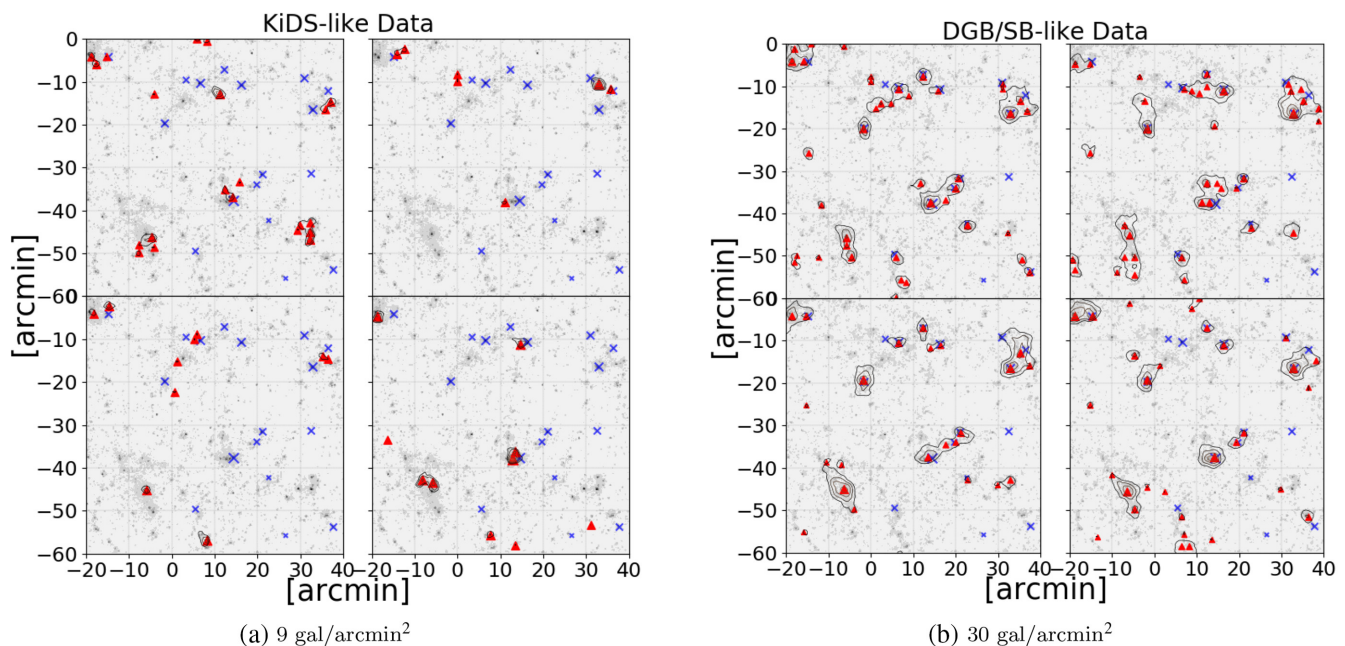


Figure 9. The correspondence between the locations of S/N peaks and massive dark matter haloes for four sets of shape noise realizations for KiDS and DGB/SB surveys. The grey scale is the true noiseless convergence map of the simulation. The contours and triangles are the aperture mass S/N and S/N peaks (≥ 3), respectively. These are calculated for source shape noise $\sigma_{|e|} = 0.25$. The \times markers are the true cluster locations from the halo finder catalogue. A smaller triangle or \times corresponds to a lower S/N peak value or a higher cluster redshift, respectively. All four panels show the same field of view ($1 \times 1 \text{ deg}^2$) with the *Planck* 2015 cosmology and $M_\nu = 0.06 \text{ eV}$.

Liu & Haiman (2016), Martinet et al. (2018), where peaks are not always associated with clusters.

5.3 Filter sizes

Even though we use a fiducial filter size of 12.5 arcmin (see Martinet et al. 2018) throughout most of this paper, in this subsection we briefly illustrate the well-studied impact of filter size (e.g. Hettterscheidt et al. 2005; Schirmer et al. 2007; Martinet et al. 2018). We focus on the 0.06 eV summed neutrino mass model. In practice for a real observational survey the filter size and form would be adjusted depending on the noise properties of the survey and the science goals.

Fig. 10 shows how the S/N peak distribution varies with filter size. The lines represent $\theta_{\text{ap}} = 8.0, 10.0, 12.5,$ and 15.0 arcmin. The panels show the ratio of the S/N distributions relative to $\theta_{\text{ap}} = 12.5$ arcmin. The model used here was *Planck* 2015 cosmology, with fiducial baryonic physics and 0.06 eV summed neutrino mass. This shows that increasing aperture size suppresses the S/N peak counts for lower S/N values while boosting counts for higher values. The larger filter sizes tend to be more sensitive to larger structures (contributing more to the higher S/N values) and less sensitive to smaller structures (suppressing lower S/N counts). In other words, the larger filters smooth shape noise, reducing the number of low S/N peaks. This is consistent with works which have sought to optimize the aperture mass filter functions or have employed other optimal filtering techniques (e.g. Hennawi & Spergel 2005; Schirmer et al. 2007; Maturi et al. 2010). Martinet et al. (2018) found that a filter size of 12.5 arcmin maximizes the number of peaks above an S/N of 3 for the KiDS data. However our synthetic catalogues are not constructed in exactly the same manner. For

example we have a different intrinsic shape noise and the optimal filter size can also change as a function of number density (see Figs 6a and b).

Neutrinos and baryons have different effects on the core of haloes which could be discriminated through a filter size and shape optimization. For examples of different filter sizes see the online Appendix Figs A1–A6.

5.4 Summed neutrino mass and S/N versus cluster mass

In Section 5 we discussed how summed neutrino mass impacts the S/N peak distribution, in particular we found that increasing summed neutrino mass suppresses the high S/N peaks. In the beginning of this section (Section 5.2) we discussed how increasing summed neutrino mass tends to decrease the masses of clusters, consistent with the authors mentioned above. In this subsection we study the relationship between S/N peak values and cluster mass, and the dependence on summed neutrino mass.

First we study the correlation between S/N peaks and cluster locations. Note that given the redshift distribution of KiDS, it is not likely that clusters with redshifts above $z = 0.5$ or so will be easily detected with lensing, since the number density of background galaxies from which the shear can be estimated is low (Martinet et al. 2018). We also limit the lower bound S/N peak values to 3 for consistency with the regime dominated by clusters rather than LSS in a KiDS-like survey (Martinet et al. 2018).

The clusters and any associated S/N peak locations can then be used to investigate how well S/N peaks trace cluster mass. We do this by taking circular areas of radius 2.0 arcmin centred on cluster centres to identify nearby S/N peaks. Note that there may not be any S/N peaks within the circles (see Fig. 9). When multiple S/N peaks

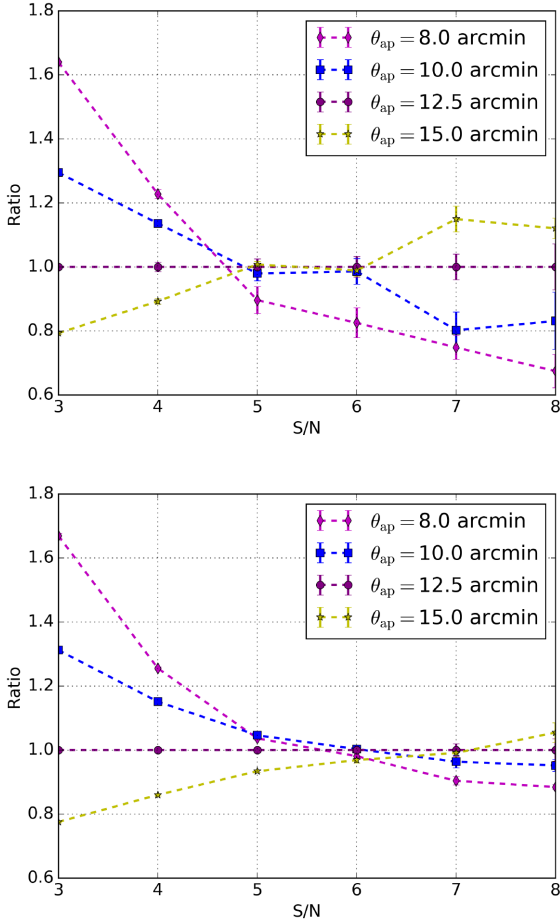


Figure 10. The ratio of the S/N distributions for various aperture sizes for KiDS and DGB/SB, top and bottom panels respectively, with respect to $\theta_{\text{ap}} = 12.5$ arcmin. The lines represent $\theta_{\text{ap}} = 8.0, 10.0, 12.5,$ and 15.0 arcmin. The error bars show the variance of the five different shape noise realizations. The model used here was *Planck* 2015 cosmology, with fiducial baryonic physics and 0.06 eV summed neutrino mass.

are enclosed, we allow for two options: either choose the closest S/N peak or the highest value enclosed. In this paper we will show only the results for choosing the closest S/N peak to a cluster,³ and allow an S/N peak to be chosen by multiple clusters.

In the case of assuming known cluster locations and choosing the closest S/N peak, in Fig. 11 we plot S/N peak values versus M_{200c} for the four different summed neutrino masses, $M_\nu = 0.06, 0.12, 0.24,$ and 0.48 eV, with the left and right panels showing the results for KiDS and DGB/SB, respectively. The line shows the mean and the error bars show the variance of S/N inside the mass bins (note that there is a limit at $S/N = 3$, which impacts on the error bars for the lower mass halo bins). Note that in these panels the clusters are not segregated into redshift bins. This means that the lensing efficiencies are not accounted for when comparing S/N peaks to cluster mass. The Pearson correlation coefficient (PCC) measures the linear relationship between two data sets, where the value can range from -1 to $+1$. $\text{PCC} = 0$ means there is no linear correlation and $+1$ (-1) means there is a positive (negative) linear

³When choosing the highest S/N peaks some points in the plot of S/N against M_{200c} are shifted to higher S/N values, but the distributions for choosing by closest and highest are mostly the same.

relationship. For KiDS the PCC values for each subpanel are (M_ν , PCC): (0.06 eV, 0.48), (0.12 eV, 0.44), (0.24 eV, 0.45), (0.48 eV, 0.37); and for DGB/SB: (0.06 eV, 0.58), (0.12 eV, 0.57), (0.24 eV, 0.55), (0.48 eV, 0.56).

To check the noise properties we have also taken the galaxy cluster positions from the FoF catalogue and compared these with random positions generated to have the same number as the S/N peaks and assigned S/N values from the distribution shown in Fig. 11(a), for each synthetic survey and summed neutrino mass. Overall the PCC values have means ~ 0 for both KiDS and DGB/SB survey characteristics.

A deeper survey gives a higher S/N peak value for a given cluster. The correlation between the peak values and mass are not significantly changed as a function of neutrino mass, even though the high end of the S/N peak distribution and the cluster mass function become suppressed with increasing summed neutrino mass (see Figs 4b, 3b, and 5). In addition the shape of the filter function will give rise to different weights for lensed galaxies at different distances from the clusters' centres where their tangential distortions will depend on the mass density profile. Even though the profiles may differ as a function of summed neutrino mass, our results indicate that although corresponding clusters might have lower masses in a higher summed neutrino mass simulation, the values of the S/N are also decreasing when the same filter is used in the measurement. Note that the simulations in these figures all have the same underlying fiducial baryonic physics. As discussed in Mummery et al. (2017) the impact of baryonic physics and summed neutrino mass on the mean halo density profiles are different on different scales. Accordingly, optimizing filter parameters that account for the impacts of baryonic physics and summed neutrino mass on S/N peak measurements is an interesting question which would require a detailed investigation outside the scope of this work.

Fig. 12 shows the S/N values versus M_{200c} for clusters segregated into different redshift bins for KiDS and DGB/SB (left-hand and right-hand panels, respectively). The simulations are for summed neutrino mass $M_\nu = 0.06$ eV. The lines are the average of the S/N values in logarithmic mass bins and the error bars show the variance of S/N inside the mass bins (note that there is a limit at $S/N = 3$, which impacts on the error bars in particular for the higher redshifts). The PCC values are (z_{bin} , PCC), for KiDS: ([0.1, 0.2], 0.62), ([0.2, 0.3], 0.71), ([0.3, 0.4], 0.66), ([0.4, 0.5], 0.54), ([0.5, 0.6], 0.21), ([0.6, 0.7], -0.09), ([0.7, 0.8], 0.26), ([0.8, 0.9], -0.20); and for DGB/SB: ([0.1, 0.2], 0.70), ([0.2, 0.3], 0.75), ([0.3, 0.4], 0.74), ([0.4, 0.5], 0.70), ([0.5, 0.6], 0.61), ([0.6, 0.7], 0.56), ([0.7, 0.8], 0.34), ([0.8, 0.9], 0.16). We have compared the relationships between galaxy cluster mass and random fields for each synthetic survey and redshift bin, where the S/N peak positions are randomized, similar to the randomization process above. The PCC values have means ~ 0 for both KiDS and DGB/SB survey characteristics. This figure shows that there is not only a greater correlation between S/N peaks and M_{200c} for the lower redshift bins, but that increasing the number density of background sources also has a significant impact on the correlation. The redshifts of the clusters enter into the calculation of the lensing convergence, while increasing the number density of background sources tends to increase the aperture mass signal. In the highest redshift bins there are fewer sources that are background to the clusters, again decreasing the lensing signal. The differences in cosmology between the different summed neutrino mass models also have a slight impact on cosmological distance measures, which enter into equation (1).

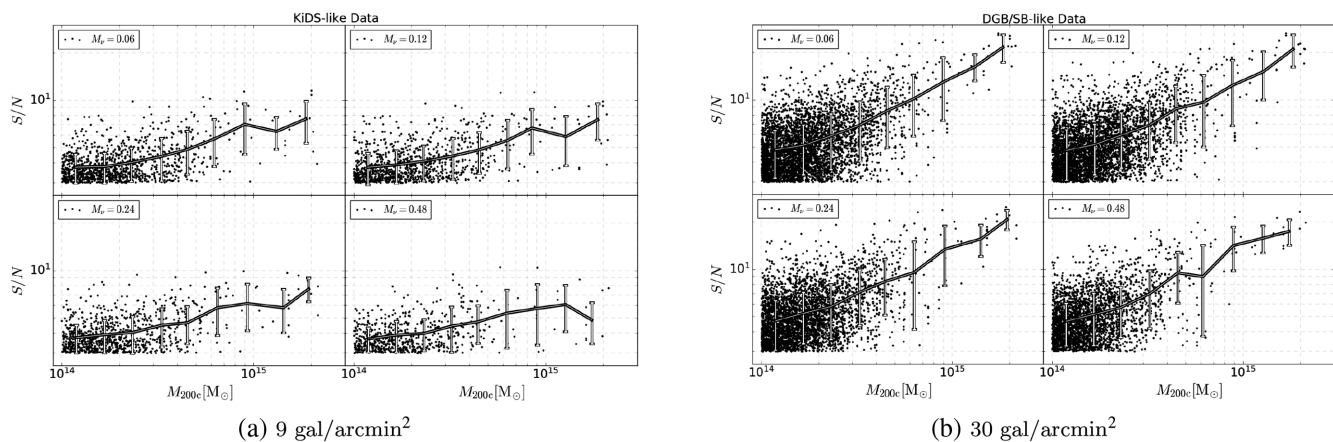


Figure 11. The S/N peaks versus M_{200c} for different summed neutrino mass for KiDS and DGB/SB (left-hand and right-hand panels, respectively). Here we use known galaxy cluster centres and find the nearest S/N peak within 2.0 arcmin. The different subpanels correspond to different summed neutrino mass $M_\nu = 0.06, 0.12, 0.24,$ and 0.48 eV. The points are the S/N values plotted against cluster mass, the line shows the mean S/N in logarithmic mass bins, and the error bars show the variance (note that there is a limit at $S/N = 3$). The PCC is calculated for each subpanel (see text for details). The PCC values for each subpanel are (M_ν, PCC) , for KiDS: $(0.06 \text{ eV}, 0.48), (0.12 \text{ eV}, 0.44), (0.24 \text{ eV}, 0.45), (0.48 \text{ eV}, 0.37)$; and for DGB/SB: $(0.06 \text{ eV}, 0.58), (0.12 \text{ eV}, 0.57), (0.24 \text{ eV}, 0.55), (0.48 \text{ eV}, 0.56)$.

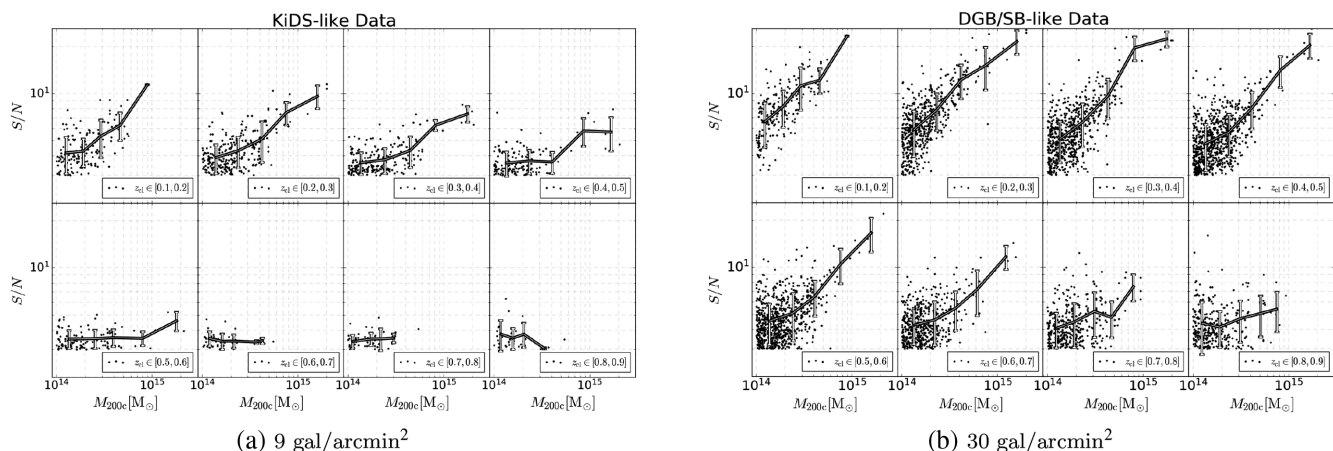


Figure 12. The S/N peaks versus M_{200c} for clusters in different redshift bins for KiDS and DGB/SB (left-hand and right-hand panels, respectively). The points are the S/N peak values (≥ 3) closest to the massive objects within 2.0 arcmin; the lines are the average of the S/N values in logarithmic mass bins and the error bars show the variance (note that there is a limit at $S/N = 3$). This plot is for $M_\nu = 0.06$ eV. The PCC values are $(z_{\text{bin}}, \text{PCC})$, for KiDS: $([0.1, 0.2], 0.62), ([0.2, 0.3], 0.71), ([0.3, 0.4], 0.66), ([0.4, 0.5], 0.54)$; for DGB/SB: $([0.1, 0.2], 0.70), ([0.2, 0.3], 0.75), ([0.3, 0.4], 0.74), ([0.4, 0.5], 0.70)$.

A similar study can be done by keeping a fixed value of summed neutrino mass while varying baryonic physics prescriptions. In the case of BAHAMAS, the low and high AGN feedback models are extreme cases, but a broader range of mass density profiles could be explored using the halo model.

5.5 Correlation between high S/N peaks and massive clusters for various source population characteristics

In this subsection we present results on the correspondence between high S/N peaks and clusters determined for different source population characteristics (KiDS, DGB/SB, and DSB) with $M_\nu = 0.06$ eV. For particular survey characteristics, ray-tracing through simulations with a reasonable prescription for baryonic physics and

summed neutrino mass can be used to establish the correlation between S/N peaks and clusters or other features in the LSS.

Fig. 13 is the S/N peak distribution for KiDS, DGB/SB, and DSB (the triangle, circle, and square markers, respectively). The error bars are the variance in the S/N bins for different noise realizations. Note that the error bars are small. As n_{eff} increases, the number of S/N peaks is significantly increased for $S/N \geq 3$. Furthermore, an increase in the number density of background sources can produce extremely high S/N peak values. Note that the filter function that we use downweights the strong lensing regime when centred on a cluster (equation 11 and Fig. 1). In practice we would also apply corrections for factors such as intrinsic alignment of galaxies, and the boost factor in dense regions, as in for example Kacprzak et al. (2016) and Martinet et al. (2018).

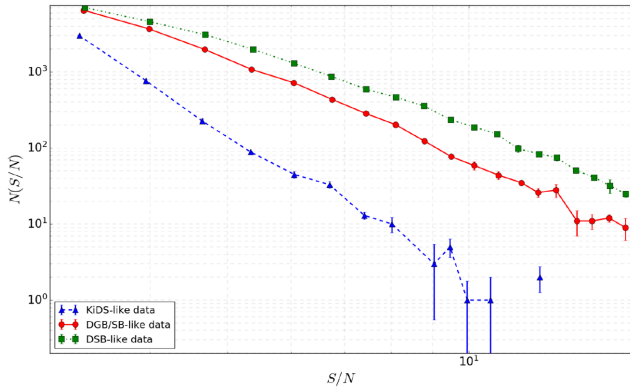


Figure 13. The high S/N peak distributions for $n_{\text{eff}} = 9, 30,$ and 60 gal arcmin^{-2} (the triangle, circle, and square markers, respectively). The error bars are the variance in the S/N bins for different noise realizations. Note that in some of the high S/N KiDS-like bins there are no detected peaks.

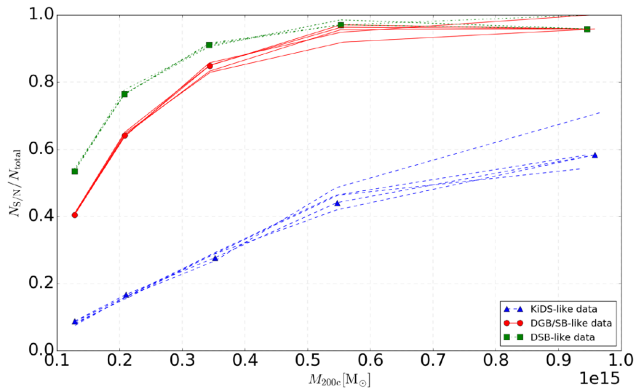


Figure 14. The fraction of clusters that have an associated S/N peak, within a radius of 2.0 arcmin from the cluster centre, as a function of cluster mass. Source number densities $n_{\text{eff}} = 9, 30,$ and 60 gal arcmin^{-2} are represented by the triangle, circle, and square markers, respectively. Here we show the results for five different shape noise realizations of background galaxies to indicate the variation that would be expected over surveys of the same area.

Fig. 14 shows the fraction of cluster-mass objects in our catalogue that enclose an S/N peak (≥ 3) within radius 2.0 arcmin, or $N_{\text{S/N}}/N_{\text{total}}$. KiDS, DGB/SB, and DSB are represented by the triangle, circle, and square markers, respectively.

Here we show the results for five different noise realizations of background galaxies.

Increasing source number density increases the ability to detect clusters with WL peaks and the overall number of S/N peaks (see Fig. 13). Therefore there are more high S/N peaks being produced around galaxy clusters, i.e. the number of S/N peaks for massive haloes tends to increase (see Fig. 11a, $M_\nu = 0.06$ eV). In the online Appendix we check the statistical significance of these results by relating galaxy cluster masses and S/N peaks at random positions, in Fig. A7.

Fig. 15 is the number of S/N peaks (≥ 3) that have a nearby halo ($\geq 10^{14} M_\odot$) within 2.0 arcmin, divided into S/N bins. The different galaxy number densities $n_{\text{eff}} = 9, 30,$ and 60 gal arcmin^{-2} are represented by the triangle, circle, and square markers, respectively. We show the results for five different noise realizations of background galaxies to indicate the variation that would be expected over surveys of the same area.

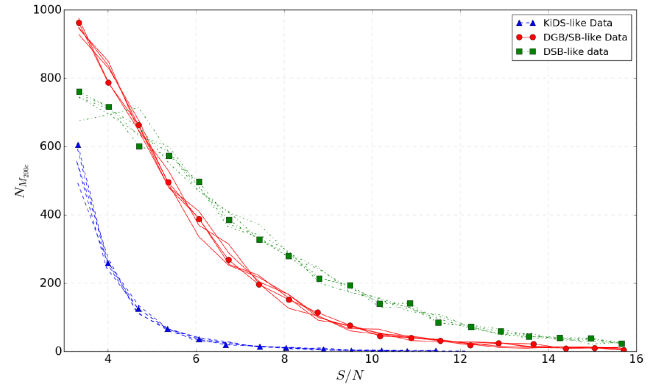


Figure 15. The number of S/N peaks (≥ 3) that have a nearby cluster within radius 2.0 arcmin, for different background galaxy number densities $n_{\text{eff}} = 9, 30,$ and 60 gal arcmin^{-2} (represented by the triangle, circle, and square markers, respectively). Here we show the results for five different shape noise realizations of background galaxies to indicate the variation that would be expected over surveys of the same area.

For the deeper data massive objects below the mass cutoff threshold could produce S/N peaks at the lower end of the range. We also consider a lower mass cutoff threshold and the number of galaxy clusters detected using a blind WL survey increases with background galaxy number density for high S/N bins.

6 CONCLUSIONS

In this paper we have quantified the impact of baryonic physics and massive neutrinos on WL peak statistics. We have considered a range of prescriptions for the baryonic physics (with zero neutrino mass) and summed neutrino mass ($M_\nu = 0.06, 0.12, 0.24, 0.48$ eV, for the fiducial baryonic physics model) implemented in the BAHAMAS simulations McCarthy et al. (2018). Our results for baryonic physics and massive neutrinos can guide the error budget when deriving cosmological parameters from WL peak statistics. We have also considered the correspondence between high S/N peaks and galaxy clusters for a fiducial baryonic physics prescription, while varying summed neutrino mass.

The WL peak statistics were determined from synthetic aperture mass S/N maps calculated from shape noise realizations of simulated WL data fields. Calculation of the convergence assumed different source redshift distributions from Chang et al. (2013) for LSST and from Hildebrandt et al. (2017) and de Jong et al. (2017) for KiDS. We use source number densities of 9 and 30 gal arcmin^{-2} , roughly corresponding to the KiDS data and the expectation for LSST and *Euclid*. We also considered a higher source number density of 60 gal arcmin^{-2} corresponding to space-based observations, such as *HST*. Aperture mass S/N maps were determined with the publicly available code from Bard et al. (2013), using the aperture mass filter function optimized to the NFW profile (Schirmer et al. 2007). We use a fiducial filter size of 12.5 arcmin for consistency with Martinet et al. (2015).

In summary we find the following:

- (i) Considering the *WMAP* 9 cosmology, the impact of baryonic physics (in addition to the gravity of DM) boosts (suppresses) the peak counts for low (high) S/N. The low S/N peaks are consistently boosted by less than a few per cent with the KiDS survey, whereas for deeper DGB/SB data the low S/N peaks are boosted by about 2–6 per cent relative to DMONLY case. With DGB/SB number

density, the lower S/N peak statistics are more sensitive to baryonic physics. The high S/N peaks become more suppressed with increasing S/N value. We explain this suppression using the fact that AGN feedback changes the shape of the mass density profiles of massive clusters. Baryonic physics is roughly degenerate with the impact of S_8 seen in Martinet et al. (2018) as well as with massive neutrinos.

(ii) During the early epoch of the Universe, free-streaming neutrinos hinder formation of LSS and result in decreasing S_8 (measured today) and, therefore, impact the WL peak distribution. For the *WMAP* 9 cosmology 0.06 and 0.12 eV summed neutrino mass models, the impact of massive neutrinos (at fixed fiducial baryonic physics) on the peak counts compared with DMONLY (collisionless dynamics) tends to be less significant or similar to that of baryonic physics. For higher 0.24 and 0.48 eV summed neutrino mass models, the impact of massive neutrinos tends to be greater than that of baryonic physics. The lowest source density (9 gal arcmin⁻²) peak distributions for the 0.06 and 0.12 eV models are not substantially different (see discussion of S_8 above and summary item below), but higher summed neutrino mass models become more distinguishable from the DMONLY model, even at this low source number density. For deeper surveys the peak distributions have greater power to differentiate between summed neutrino mass models.

(iii) Different cosmological parameters based on *WMAP* 9 and *Planck* 2015 surveys were compared, using models with summed neutrino mass 0.06, 0.12, 0.24, and 0.48 eV, all with fiducial baryonic physics. In comparison with *WMAP* 9 fiducial baryonic physics with massless neutrinos, the peak distributions show clear differences for the *WMAP* 9 and *Planck* 2015 cosmologies if restricted to the 0.06 and 0.12 eV models; at low S/N the peak distributions of *Planck* 2015 are consistently suppressed by less than ~ 5 per cent for the 30 gal arcmin⁻² source number density case, and the high S/N peaks are boosted by ~ 5 to ~ 10 per cent, compared to the *WMAP* 9 peak distributions. Overall the trends in the WL peak counts are ordered with respect to S_8 , see Table 1. For example, in models across cosmologies but with similar S_8 values the peak counts are difficult to distinguish. The *WMAP* 9 $M_\nu = 0.00$ (0.24) eV model has similar peak counts to the *Planck* 2015 $M_\nu = 0.24$ (0.48) eV model, respectively.

Note that since neutrinos change the formation of structure, for example impacting on the measured σ_8 , whereas for massive haloes baryons primarily alter the mass density profiles, ordering in WL peak counts as a function of S_8 is not seen for models with different baryonic physics. For example, although our *WMAP* 9 AGN low, fiducial, and high models have the same S_8 they do not have the same WL peak distributions.

(iv) Impact of massive neutrinos on high S/N peaks and massive clusters: consistent with Costanzi et al. (2013), Castorina et al. (2014), Mummery et al. (2017), Hagstotz et al. (2019), the cluster mass function is reduced in amplitude when including baryonic physics and non-zero neutrino mass. For a fixed prescription of baryonic physics in the *Planck* 2015 cosmology, higher neutrino mass reduces the number of high S/N peaks. Increasing the summed neutrino mass typically, although not always, reduces the masses and S/N peak heights of individual galaxy clusters.

(v) Detecting peaks around galaxy clusters within a radius of 2.0 arcmin, for $M_\nu = 0.06$ eV, and with fiducial baryonic physics: even for the most massive clusters ($\geq 10^{14} M_\odot$), a WL S/N peak is not always present at the lowest source number density, 9 gal arcmin⁻². For example, in Fig. 14, at $M_{200c} \approx 6 \times 10^{14} M_\odot$ there is ≈ 50 per cent likelihood that a cluster has a corresponding WL peak, with $S/N \geq 3$. At higher source number density

(30 gal arcmin⁻²) we find that more than 90 per cent of clusters have a detected WL peak. For the highest number density 60 gal arcmin⁻², we find that nearly all clusters have a detected WL peak. Note that the initially random distribution of intrinsic background galaxy shapes from which the shear is measured has an impact on the detection of a foreground cluster using aperture mass peaks. The ability to study the peak statistics for intermediate redshift galaxy clusters relies on deeper lensing data, as can be seen in the differences between Figs 12(a) and (b). Increasing the source number density increases the overall number of higher S/N peaks, and for deeper data other features such as projections of large-scale structure and combinations of lower mass haloes can also be significantly detected. With higher source number density the overall number of detected galaxy clusters increases. These statements on cluster detection with WL peaks for different source number densities hold for the range of summed neutrino masses considered. However, the number of clusters decreases as a function of summed neutrino mass.

(vi) Fig. 7 and Table 2 encapsulate the main findings of this paper. For the *WMAP* 9 cosmology, the percentage difference between the S/N peak counts in comparison with the DMONLY (collisionless dynamics) model is shown for summed neutrino mass 0.00, 0.06, 0.12, 0.24, and 0.48 eV models (all with fiducial baryonic physics). Assuming that baryonic physics and massive neutrinos act independently (Mummery et al. 2017): for lower (non-zero) summed neutrino mass models 0.06 and 0.12 eV, baryonic physics tends to have a greater or similar impact on the results than massive neutrinos; for higher summed neutrino mass models 0.24 and 0.48 eV, massive neutrinos can change the peak counts by more than fiducial baryonic physics. We have considered a range of models for baryonic physics and summed neutrino mass; the precise impact will depend on the true baryonic physics and summed neutrinos mass, as well as on the characteristics of the survey itself. A detailed study of baryonic physics and massive neutrinos (impacting on mass density profiles and halo formation) would be possible in the framework of the halo model.

We look forward to applying the results of this theoretical work to observational data, such as the LSST and *Euclid* surveys. Here we have considered the synthetic peak counts on the sky, independent of redshift. More precise predictions for the peak statistics can also be made accounting for tomographic information in surveys, and the ability to break degeneracies between baryonic physics, massive neutrinos, and other cosmological parameters can be studied.

ACKNOWLEDGEMENTS

MF, MC, and LJK acknowledge support for this work from the National Science Foundation, grant number 1517954. BL acknowledges support for this work by National Aeronautics and Space Administration, grant number NNX16AF53G. VC was supported during part of this work by the Clark Summer Program at The University of Texas at Dallas. RB acknowledges support from the National Science Foundation Research Experiences for Undergraduates program at the Maria Mitchell Observatory. We thank Regina Jorgenson for advising RB at Maria Mitchell Observatory's REU program and for helpful discussions. We thank Mike Kesen for helpful discussions. We thank the Texas Advanced Computer Center for use of resources, and NVIDIA for donating a GPU for our computations. IGM thanks Simeon Bird and Joop Schaye for their contributions to the BAHAMAS simulations. This project has received funding from the European Research

Council (ERC) under the European Union's Horizon 2020 research and innovation programme (grant agreement number 769130). AP acknowledges support from an Enhanced Eurotalents Fellowship, a Marie Skłodowska-Curie Actions Programme co-funded by the European Commission and Commissariat à l'énergie atomique et aux énergies alternatives (CEA). We thank the referee for a detailed and insightful report that has improved the manuscript.

This research made use of *ASTROPY*,⁴ a community-developed core Python package for Astronomy (Astropy Collaboration et al. 2013, 2018). Plots in this paper were produced with *PYTHON* and its *MATPLOTLIB* (Hunter 2007).

REFERENCES

- Addison G. E., Huang Y., Watts D. J., Bennett C. L., Halpern M., Hinshaw G., Weiland J. L., 2016, *ApJ*, 818, 132
- Allen S. W., Evrard A. E., Mantz A. B., 2011, *ARA&A*, 49, 409
- Amendola L. et al., 2018, *Living Rev. Relativ.*, 21, 2
- Astropy Collaboration et al., 2013, *A&A*, 558, A33
- Astropy Collaboration et al., 2018, *AJ*, 156, 123
- Bard D., Bellis M., Allen M. T., Yepremyan H., Kratochvil J. M., 2013, *Astronomy and Computing*, 1, 17
- Bartelmann M., 1996, *A&A*, 313, 697
- Bartelmann M., Schneider P., 2001, *Phys. Rep.*, 340, 291
- Bashinsky S., Seljak U., 2004, *Phys. Rev. D*, 69, 083002
- Battye R. A., Moss A., 2014, *Phys. Rev. Lett.*, 112, 051303
- Bird S., Viel M., Haehnelt M. G., 2012, *MNRAS*, 420, 2551
- Blumenthal G. R., Faber S. M., Primack J. R., Rees M. J., 1984, *Nature*, 311, 517
- Bond J. R., Efstathiou G., Silk J., 1980, *Phys. Rev. Lett.*, 45, 1980
- Castorina E., Sefusatti E., Sheth R. K., Villaescusa-Navarro F., Viel M., 2014, *J. Cosmol. Astropart. Phys.*, 2014, 049
- Castro T., Quartin M., Giocoli C., Borgani S., Dolag K., 2018, *MNRAS*, 478, 1305
- Chang C. et al., 2013, *MNRAS*, 434, 2121
- Clowe D., De Lucia G., King L., 2004, *MNRAS*, 350, 1038
- Costanzi M., Villaescusa-Navarro F., Viel M., Xia J.-Q., Borgani S., Castorina E., Sefusatti E., 2013, *J. Cosmol. Astropart. Phys.*, 2013, 012
- Cusworth S. J., Kay S. T., Battye R. A., Thomas P. A., 2014, *MNRAS*, 439, 2485
- Davies C., Cautun M., Li B., 2019, preprint (arXiv:1905.01710)
- de Jong J. T. A. et al., 2017, *A&A*, 604, A134
- Dietrich J. P., Hartlap J., 2010, *MNRAS*, 402, 1049
- Di Valentino E., Melchiorri A., Linder E. V., Silk J., 2017, *Phys. Rev. D*, 96, 023523
- Dolag K., Borgani S., Murante G., Springel V., 2009, *MNRAS*, 399, 497
- Dubois Y. et al., 2014, *MNRAS*, 444, 1453
- Fan Z., Shan H., Liu J., 2010, *ApJ*, 719, 1408
- Feeney S. M., Mortlock D. J., Dalmaso N., 2018, *MNRAS*, 476, 3861
- Gratton S., Lewis A., Efstathiou G., 2008, *Phys. Rev. D*, 77, 083507
- Hagstotz S., Costanzi M., Baldi M., Weller J., 2019, *MNRAS*, 486, 3927
- Hamana T., Oguri M., Shirasaki M., Sato M., 2012, *MNRAS*, 425, 2287
- Hamana T., Takada M., Yoshida N., 2004, *MNRAS*, 350, 893
- Hannestad S., Tu H., Wong Y. Y., 2006, *J. Cosmol. Astropart. Phys.*, 2006, 025
- Hennawi J. F., Spergel D. N., 2005, *ApJ*, 624, 59
- Henson M. A., Barnes D. J., Kay S. T., McCarthy I. G., Schaye J., 2017, *MNRAS*, 465, 3361
- Hetterscheidt M., Erben T., Schneider P., Maoli R., van Waerbeke L., Mellier Y., 2005, *A&A*, 442, 43
- Heymans C. et al., 2012, *MNRAS*, 427, 146
- Hildebrandt H., Viola M., Heymans C., Joudaki S., Kuijken K., Blake C., Erben T., Joachimi B., 2017, *MNRAS*, 465, 1454
- Hinshaw G. et al., 2013, *ApJ*, 208, 19
- Hu W., Eisenstein D. J., Tegmark M., 1998, *Phys. Rev. Lett.*, 80, 5255
- Hunter J. D., 2007, *Comput. Sci. Eng.*, 9, 90
- Jain B., Waerbeke L. V., 2000, *ApJ*, 530, L1
- Kacprzak T. et al., 2016, *MNRAS*, 463, 3653
- King L. J. et al., 2016, *MNRAS*, 459, 517
- Kratochvil J. M., Haiman Z., May M., 2010, *Phys. Rev. D*, 81, 043519
- Kravtsov A. V., Borgani S., 2012, *ARA&A*, 50, 353
- Kruse G., Schneider P., 1999, *MNRAS*, 302, 821
- Kruse G., Schneider P., 2000, *MNRAS*, 318, 321
- Lahav O., Kiakotou A., Abdalla F. B., Blake C., 2010, *MNRAS*, 405, 168
- Laureijs R. et al., 2011, preprint (arXiv:1110.3193)
- Le Brun A. M. C., McCarthy I. G., Schaye J., Ponman T. J., 2014, *MNRAS*, 441, 1270
- Lee B. E., Le Brun A. M. C., Haq M. E., Deering N. J., King L. J., Applegate D., McCarthy I. G., 2018, *MNRAS*, 479, 890
- Leonard A., Pires S., Starck J.-L., 2012, *MNRAS*, 423, 3405
- Lesgourgues J., Pastor S., 2006, *Phys. Rep.*, 429, 307
- Lesgourgues J., Pastor S., 2012, *Advances in High Energy Physics*, 2012, 608515
- Lin C.-A., Kilbinger M., 2015, *A&A*, 583, A70
- Liu J., Haiman Z., 2016, *Phys. Rev. D*, 94, 043533
- Liu J., Madhavacheril M. S., 2019, *Phys. Rev. D*, 99, 083508
- Liu X. et al., 2016, *Phys. Rev. Lett.*, 117, 051101
- Li Z., Liu J., Matilla J. M. Z., Coulton W. R., 2019, *Phys. Rev. D*, 99, 063527
- Martinet N., Bartlett J. G., Kiessling A., Sartoris B., 2015, *A&A*, 581, A101
- Martinet N. et al., 2018, *MNRAS*, 474, 712
- Massara E., Villaescusa-Navarro F., Viel M., 2014, *J. Cosmol. Astropart. Phys.*, 2014, 053
- Maturi M., Angrick C., Pace F., Bartelmann M., 2010, *A&A*, 519, A23
- McCarthy I. G., Bird S., Schaye J., Harnois-Deraps J., Font A. S., van Waerbeke L., 2018, *MNRAS*, 476, 2999
- McCarthy I. G., Schaye J., Bird S., Le Brun A. M. C., 2017, *MNRAS*, 465, 2936
- Mead A. J., Heymans C., Lombriser L., Peacock J. A., Steele O. I., Winther H. A., 2016, *MNRAS*, 459, 1468
- Moscardini L., Baldi M., Giocoli C., 2018, *MNRAS*, 481, 2813
- Mummery B. O., McCarthy I. G., Bird S., Schaye J., 2017, *MNRAS*, 471, 227
- Namikawa T., Saito S., Taruya A., 2010, *J. Cosmol. Astropart. Phys.*, 2010, 027
- Osato K., Shirasaki M., Yoshida N., 2015, *ApJ*, 806, 186
- Peel A., Lin C.-A., Lanusse F., Leonard A., Starck J.-L., Kilbinger M., 2017, *A&A*, 599, A79
- Peel A., Pettorino V., Giocoli C., Starck J.-L., Baldi M., 2018, *A&A*, 619, A38
- Pillepich A. et al., 2018, *MNRAS*, 473, 4077
- Planck Collaboration LI, 2017, *A&A*, 607, A95
- Planck Collaboration VI, 2018, preprint (arXiv:1807.06209)
- Planck Collaboration XIII, 2016a, *A&A*, 594, A13
- Planck Collaboration XVI, 2016b, *A&A*, 594, A16
- Poulin V., Boddy K. K., Bird S., Kamionkowski M., 2018, *Phys. Rev. D*, 97, 123504
- Riess A. G. et al., 2018, *ApJ*, 855, 136
- Roncarelli M., Carbone C., Moscardini L., 2015, *MNRAS*, 447, 1761
- Sawala T., Frenk C. S., Crain R. A., Jenkins A., Schaye J., Theuns T., Zavala J., 2013, *MNRAS*, 431, 1366
- Schaller M. et al., 2015, *MNRAS*, 452, 343
- Schaye J. et al., 2010, *MNRAS*, 402, 1536
- Schaye J. et al., 2015, *MNRAS*, 446, 521
- Schirmer M., Erben T., Hetterscheidt M., Schneider P., 2007, *A&A*, 462, 875
- Schneider A., Teyssier R., 2015, *J. Cosmol. Astropart. Phys.*, 12, 049

⁴<http://www.astropy.org>

- Schneider P., 1996, *MNRAS*, 283, 837
- Schneider P., 2005, in Meylan G., Jetzer P., North P., eds, Gravitational Lensing: Strong, Weak & Micro. Lecture Notes of the 33rd Saas-Fee Advanced Course. Springer-Verlag, Berlin, p. 273
- Schneider P., van Waerbeke L., Jain B., Kruse G., 1998, *MNRAS*, 296, 873
- Schrabback T. et al., 2018, *MNRAS*, 474, 2635
- Semboloni E., Hoekstra H., Schaye J., van Daalen M. P., McCarthy I. G., 2011, *MNRAS*, 417, 2020
- Shan H. et al., 2018, *MNRAS*, 474, 1116
- van Daalen M. P., Schaye J., Booth C. M., Dalla Vecchia C., 2011, *MNRAS*, 415, 3649
- Velliscig M., van Daalen M. P., Schaye J., McCarthy I. G., Cacciato M., Le Brun A. M. C., Dalla Vecchia C., 2014, *MNRAS*, 442, 2641
- Villaescusa-Navarro F., Marulli F., Viel M., Branchini E., Castorina E., Sefusatti E., Saito S., 2014, *J. Cosmol. Astropart. Phys.*, 2014, 011
- Vogelsberger M., Genel S., Sijacki D., Torrey P., Springel V., Hernquist L., 2013, *MNRAS*, 436, 3031
- Voit G. M., 2005, *Rev. Mod. Phys.*, 77, 207
- Wagner C., Verde L., Jimenez R., 2012, *ApJ*, 752, L31
- White M., Vale C., 2004, *Astropart. Phys.*, 22, 19
- Wyman M., Rudd D. H., Vanderveld R. A., Hu W., 2014, *Phys. Rev. Lett.*, 112, 051302
- Yang X., Kratochvil J. M., Huffenberger K., Haiman Z., May M., 2013, *Phys. Rev. D*, 87, 023511
- Yang X., Kratochvil J. M., Wang S., Lim E. A., Haiman Z., May M., 2011, *Phys. Rev. D*, 84, 043529

SUPPORTING INFORMATION

Supplementary data are available at [MNRAS](https://www.mnras.org) online.

Figure A1. The impact of baryonic processes on the WL peak statistics with different aperture filter sizes shown in the three subpanels.

Figure A2. The impact of varying neutrino mass on the WL peak statistics for different filter sizes shown in the three subpanels.

Figure A3. The impact of *WMAP* 9 and *Planck* 2015 cosmologies with summed neutrino mass of 0.06 and 0.12 eV on the WL peak statistics for different filter sizes shown in the three subpanels.

Figure A4. The impact of baryonic processes on the WL peak statistics for different filter sizes shown in the three subpanels.

Figure A5. The impact of varying neutrino mass on the WL peak statistics for different filter sizes shown in the three subpanels.

Figure A6. The impact *WMAP* 9 and *Planck* 2015 cosmologies with summed neutrino mass of 0.06 and 0.12 eV on the WL peak statistics for different filter sizes shown in the three subpanels.

Figure A7. We show the fraction of haloes that have a randomized S/N peak position within 2.0 arcmin, as a function of cluster mass.

Please note: Oxford University Press is not responsible for the content or functionality of any supporting materials supplied by the authors. Any queries (other than missing material) should be directed to the corresponding author for the article.

APPENDIX A: ADDITIONAL PEAK DISTRIBUTIONS

Here, we present the other comparisons of WL peak distributions, referred to in Section 5.1, including varying filter sizes. In the main text, our discussions focus on the plots with filter size $\theta_{\text{ap}} = 12.5$ arcmin. The error bars are the standard deviation of the five different shape noise realizations.

For online Fig. A7 we follow the same randomization process mentioned in Section 5.5 for Fig. 14. This plot shows the relationship between galaxy cluster locations and a random noise field, with the same number of random positions as S/N peaks from the original synthetic survey data. The fraction $N_{\text{S/N}}/N_{\text{total}}$ increases with source number density because the total number of high S/N peaks are increased (see Fig. 13). The synthetic DGB/SB and DSB fractions extend to higher mass bins due to the fact that there are more high S/N peaks in these surveys, and that high galaxy cluster masses are more rare. The relatively flat relationships shown here illustrates that the results in Fig. 14 are not due to random noise.

This paper has been typeset from a $\text{\TeX}/\text{\LaTeX}$ file prepared by the author.